NASA Technical Paper 1924

Comparison of Data Inversion Techniques for Remotely Sensed Wide-Angle Observations of Earth Emitted Radiation

Richard N. Green

DECEMBER 1981

NASA

NASA Technical Paper 1924

Comparison of Data Inversion Techniques for Remotely Sensed Wide-Angle Observations of Earth Emitted Radiation

Richard N. Green
Langley Research Center
Hampton, Virginia

NASA
National Aeronautics
and Space Administration

**Scientific and Technical
Information Branch**

1981

CONTENTS

INTRODUCTION 1

SYMBOLS 2

THEORY 3
Formulation of Problem for Emitted Radiation 3
Shape Factor Technique 5
Parameter Estimation Technique 7
Deconvolution Technique 8

IMPLEMENTATION OF TECHNIQUES 9
Field Representations 9
Transformation Between Regions and Spherical Harmonics 11
Relationship Between Region Size and Spherical Harmonic Representation 13
Calculation of Important Parameters 14

APPLICATION OF TECHNIQUES TO DATA SET 16
Earth Radiation Data 16
Shape Factor Technique 17
Parameter Estimation Technique 20
Deconvolution Technique 23

COMPARISON OF TECHNIQUES 26

CONCLUSIONS 33

APPENDIX A - SPHERICAL HARMONIC COEFFICIENTS FROM REGIONAL VALUES 35

APPENDIX B - 10° × 10° REGIONAL VALUES FROM 10° × 20° REGIONAL VALUES 38

APPENDIX C - SPECTRUM OF A RANDOM FIELD 40

REFERENCES 42

INTRODUCTION

For many years, observations of the Earth radiation budget have been made from orbiting satellites. These observations can be analyzed by suitable techniques to estimate the radiant exitance field at the top of the atmosphere. A number of such data analysis techniques are available, each with its own simplifying assumptions and characteristics which affect the derived radiant exitance. In the past, there has been some consideration of how errors in measurements and errors associated with a given technique affect the derived radiant exitance. However, little emphasis has been placed on the differences between the techniques themselves and how these differences affect the derived radiant exitances. In the present study the effect on the radiant exitance estimates of analyzing the same data with three techniques is examined.

The longwave component of the Earth radiation budget, measured by a wide field of view radiometer aboard an orbiting satellite, has been chosen as the data type for this study. Each measurement is an integral of the irradiance from all points within the field of view weighted by the directional response of the sensor. The shape factor technique has been the most popular way to solve this integral measurement equation. Each measurement is divided by a scaler to derive the radiant exitance at the top of the atmosphere. With another approach, the parameter estimation technique, all measurements are processed together as a batch and the radiant exitance estimate is defined as a least squares fit to the data. With the third approach, the deconvolution technique, use is made of the fact that spherical harmonics are the eigenfunctions of the integral measurement operator. These three techniques are studied by applying them to the same set of radiation data and comparing the resulting radiant exitances on a global, zonal, and 10° regional scale.

Details of the technique derivations and implementations are very important to understanding the results. For this reason the basic measurement equation which relates the measurements to the derived radiant exitance is formulated. Each technique is derived from this equation, and the associated assumptions are set forth. In addition, each technique has its own unique implementation. For example, the results of the shape factor technique depend on the size of the surface area over which point estimates are averaged to produce regional estimates. The parameter estimation results are affected by the numerical integration scheme employed and by the model of the radiation directional function. The deconvolution results also are a function of this model and in addition vary with the degree of truncation of the spherical harmonic representation. Each of these aspects of the techniques is investigated by means of numerical examples and discussed. The results of the deconvolution technique are in terms of spherical harmonics, while the results of the other two techniques are regional radiant exitances. To compare these three techniques, their results must be transformed to the same coordinate system, and the transformation also affects the results. Finally, we examine the advantages and disadvantages of each data analysis technique.

SYMBOLS

a_n^m, b_n^m	complex coefficients of spherical harmonics, $W\text{-}m^{-2}$
A	area, km^2
A_g	area of globe, km^2
B	matrix of influence coefficients (see eq. (13))
B_{ik}	influence of radiant exitance of kth region on ith measurement
C_m, S_m, I_n^m	integrals defined by equations (27) through (29)
C_n^m, S_n^m	real coefficients of spherical harmonics, $W\text{-}m^{-2}$
F	shape factor (see eq. (7))
h	satellite altitude above R_e, km
K	total number of regions
L	Earth-emitted radiance, $W\text{-}m^{-2}\text{-}sr^{-1}$
$\mathcal{L}$	measurement operator
m	measured radiation at satellite altitude, $W\text{-}m^{-2}$
M	radiant exitance, $W\text{-}m^{-2}$
N	degree of truncation; also, number of measurements
N_n^m	normalizing coefficients for spherical harmonics
P_n^m	associated Legendre polynomial of degree n and order m
r	distance from surface element to satellite, km
R	directional function, sr^{-1}
R_e	radius of Earth-atmosphere system, km
$S(\alpha)$	angular response of sensor
X	arbitrary real function on the surface of a sphere
Y_{cn}^m, Y_{sn}^m	real spherical harmonics of degree n and order m
Y_n^m	complex spherical harmonic of degree n and order m
α	cone angle at satellite from satellite nadir to point on surface of Earth
α_h	cone angle to horizon

β clock angle from north about the satellite nadir to point on surface of Earth

β_n smoothing parameter (see eq. (31))

γ Earth central angle

γ^* angular radius of a circular region

δ_n^m Kronecker delta function

θ zenith angle

Θ colatitude

λ_n nth eigenvalue of measurement operator

ρ regional correlation coefficient

$\rho(\gamma)$ weighting function

σ^2 variance of random variable

σ_n degree dispersion, $W\text{-}m^{-2}$ (see eq. (39))

ϕ azimuth

Φ longitude

Ω solid angle, sr

Subscript:

s satellite

Abbreviations:

FOV field of view

LD limb darkening

Lamb Lambertian

A circumflex ($\hat{}$) over a symbol denotes an estimate. A tilde ($\sim$) over a symbol denotes the smoothed radiant exitance field.

THEORY

Formulation of Problem for Emitted Radiation

The surface at the top of the Earth-atmosphere system is approximated by a sphere of radius R_e. The Earth-emitted radiance L leaving any point on this spherical surface is modeled as a function of colatitude Θ, longitude Φ, and zenith

angle θ of the exiting ray and is not a function of azimuth ϕ (see fig. 1). The radiant exitance M at a point on this surface is given by

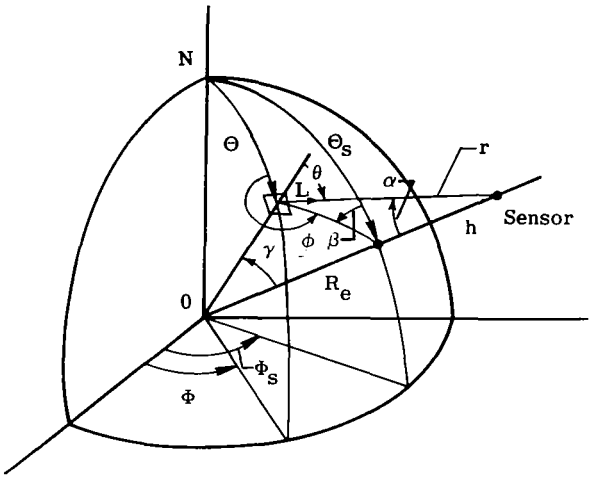

Figure 1.- Earth-satellite geometry.

$$M(\Theta,\Phi) = \int_{\phi=0}^{2\pi} \int_{\theta=0}^{\pi/2} L(\Theta,\Phi,\theta) \cos\theta \sin\theta \, d\theta \, d\phi$$

or

$$M(\Theta,\Phi) = 2\pi \int_{\theta=0}^{\pi/2} L(\Theta,\Phi,\theta) \cos\theta \sin\theta \, d\theta \tag{1}$$

A radiation directional function for emitted radiation $R(\Theta,\Phi,\theta)$, the limb darkening function, is defined so that

$$L(\Theta,\Phi,\theta) \equiv \frac{1}{\pi} M(\Theta,\Phi) \, R(\Theta,\Phi,\theta) \tag{2}$$

In order for equations (1) and (2) to be compatible, R must satisfy the normalizing condition,

$$2 \int_{\theta=0}^{\pi/2} R(\Theta,\Phi,\theta) \cos\theta \sin\theta \, d\theta = 1 \tag{3}$$

For this study R is assumed to have no azimuthal dependence. If the surface is Lambertian and radiates with equal intensity in all directions, then $R(\Theta,\Phi,\theta) = 1$.

Now consider a radiation sensor at satellite altitude, as shown in figure 1. In modeling the satellite measurements, we do not consider measurement errors or time variation of the radiation field. Thus, the radiance from the top of the Earth-atmospheric system incident on the sensor at a colatitude Θ_s, longitude Φ_s, and altitude h is modeled as

$$m(\Theta_s,\Phi_s,h) = \int_{FOV} L(\Theta,\Phi,\theta)\ S(\alpha)\ d\Omega \tag{4}$$

where θ is a function of the locations of the satellite (Θ_s,Φ_s) and of the surface element at the top of the atmosphere (Θ,Φ), Ω is the solid angle at the satellite subtended by the surface element, α is the nadir angle at the satellite from the local vertical to the surface element, and the integration is carried out over the field of view (FOV) which depends on Θ_s, Φ_s, and h. The function $S(\alpha)$ is the angular response of the sensor to incoming radiation. This angular response function could be expanded to incorporate the geometry of other types of sensors as well as to incorporate a dependence on azimuth. However, in this study a perfectly black flat-plate sensor normal to the vertical is assumed for which $S(\alpha) = \cos\ \alpha$. By use of equation (2), equation (4) may be written

$$m(\Theta_s,\Phi_s,h) = \frac{1}{\pi} \int_{FOV} M(\Theta,\Phi)\ R(\Theta,\Phi,\theta)\ \cos\ \alpha\ d\Omega \tag{5}$$

which relates the known measurement m to the unknown radiant exitance M.

Shape Factor Technique

Many investigators (e.g., Smith et al. 1977, Jacobowitz et al. 1979, Weaver and House 1979) have used the shape factor technique (also called inverse square law) to transform wide field of view radiation measurements at satellite altitude to estimates of the radiant exitance at the top of the atmosphere. The measurement m is divided by a geometric shape factor F to obtain the radiant exitance associated with the nadir point. The assumption is made that the radiant exitance at the top of the atmosphere is constant over the field of view, or that $M(\Theta,\Phi) = M(\Theta_s,\Phi_s)$, so that equation (5) gives

$$\hat{M}(\Theta_s,\Phi_s) = \frac{m(\Theta_s,\Phi_s,h)}{F} \tag{6}$$

where the circumflex (^) denotes an estimate and the geometric shape factor is given by

$$F = \frac{1}{\pi} \int_{FOV} R(\Theta,\Phi,\theta)\ \cos\ \alpha\ d\Omega \tag{7}$$

In most applications, the shape factor is simplified by the further assumption that the directional function is independent of position; that is, $R(\Theta,\Phi,\theta) = R(\theta)$. If the variables of integration are changed from solid angle Ω to the cone and clock angles α and β, then equation (7) becomes

$$F = \frac{1}{\pi} \int_{\beta=0}^{2\pi} \int_{\alpha=0}^{\alpha_h} R(\theta) \cos \alpha \sin \alpha \, d\alpha \, d\beta$$

or

$$F = 2 \int_{\alpha=0}^{\alpha_h} R(\theta) \cos \alpha \sin \alpha \, d\alpha \tag{8}$$

where α_h is the cone angle to the horizon, or the extent of the field of view. From figure 1 and the law of sines, the following relation is obtained:

$$\sin \alpha = \frac{R_e}{R_e + h} \sin \theta \tag{9}$$

Differentiating equation (9) gives

$$\cos \alpha \, d\alpha = \frac{R_e}{R_e + h} \cos \theta \, d\theta \tag{10}$$

Substituting equations (9) and (10) into equation (8) yields

$$F = \left(\frac{R_e}{R_e + h} \right)^2 2 \int_{\theta=0}^{\pi/2} R(\theta) \sin \theta \cos \theta \, d\theta$$

or from equation (3)

$$F = \left(\frac{R_e}{R_e + h} \right)^2$$

Thus, the geometric shape factor is independent of the directional function for the assumptions considered and is a function only of the measurement altitude h. For a circular orbit, the shape factor is constant for all measurements. Whatever the case, the shape factor technique is characterized by reducing each measurement individually from satellite altitude to a radiant exitance at the top of the atmosphere by dividing by a geometric shape factor. These individual radiant exitances are used to define the global radiant exitance field.

Parameter Estimation Technique

With the parameter estimation technique, all measurements are processed as a batch, and a global radiant exitant field at the top of the atmosphere is produced by means of a matrix inversion. Consider the surface of the globe divided into K regions, each with constant radiant exitance M_k and directional function $R_k(\theta)$ (k = 1, 2, ..., K). The measurement equation (5) can be expressed in terms of surface area instead of solid angle as

$$m(\Theta_s,\Phi_s,h) = \frac{1}{\pi} \int_{FOV} M(\Theta,\Phi)\, R(\Theta,\Phi,\theta)\, \cos\alpha\, \frac{\cos\theta}{r^2}\, dA$$

where r is the distance from the satellite to the surface element. Incorporating the assumed regional radiant exitance model gives

$$m(\Theta_s,\Phi_s,h) = \frac{1}{\pi} \sum_{k=1}^{K} M_k \int_{FOV_k} R_k(\theta)\, \cos\alpha\, \frac{\cos\theta}{r^2}\, dA$$

where the integration is over the surface area that is in both the field of view and the kth region. Thus, the ith measurement is modeled as

$$m_i = \sum_{k=1}^{K} B_{ik} M_k \qquad (i = 1, 2, \ldots, N) \qquad (11)$$

where B_{ik} is the influence coefficient of M_k on the ith measurement and is given by

$$B_{ik} = \frac{1}{\pi} \int_{FOV_{ik}} R_k(\theta_i)\, \cos\alpha_i\, \frac{\cos\theta_i}{r_i^2}\, dA \qquad (12)$$

In matrix form, the set of equations defined by equation (11) become

$$\underline{m} = B\underline{M} \qquad (13)$$

where $\underline{m}$ is a column vector of N measurements, $\underline{M}$ is a column vector of K regional radiant exitances, and B is the observational matrix with elements B_{ik}.

For a large measurement set ($N > K$) over the globe, equation (13) represents an overdetermined set of simultaneous equations which yield the least squares solution,

$$\hat{\underline{M}} = (B^T B)^{-1} B^T \underline{m} \tag{14}$$

Deconvolution Technique

The deconvolution technique, described by Smith and Green (1981) and Bess et al. (1981), can be viewed as a parameter estimation technique with a spherical harmonic basis set rather than a piecewise constant basis set. The deconvolution solution to the measurement equation (5) can be found analytically, but it requires additional assumptions. It is convenient to express the relationship between the measured radiation $m(\Theta_s,\Phi_s)$ and the unknown radiant exitance $M(\Theta,\Phi)$ as

$$m(\Theta_s,\Phi_s) = \mathcal{L}[M(\Theta,\Phi] \tag{15}$$

where $\mathcal{L}$ denotes the linear integral measurement operator of equation (5). Smith and Green (1981) have shown that the eigenfunctions of this linear operator are spherical harmonics, that is,

$$\mathcal{L}[Y_n^m(\Theta,\Phi)] = \lambda_n Y_n^m(\Theta_s,\Phi_s) \tag{16}$$

where $Y_n^m(\Theta_s,\Phi_s)$ is a spherical harmonic of order m and degree n evaluated at the subsatellite point. The associated eigenvalue λ_n is given by

$$\lambda_n = 2 \int_{\alpha=0}^{\alpha_h} P_n^0(\cos\gamma)\, R(\theta) \cos\alpha \sin\alpha \, d\alpha \tag{17}$$

where $P_n^0(\cos\gamma)$ denotes the Legendre polynomial of degree n as a function of the Earth central angle γ (see fig. 1).

Because spherical harmonics are eigenfunctions of the measurement operator, let the radiant exitance at the surface be represented by a series of spherical harmonics truncated at degree N:

$$M(\Theta,\Phi) = \sum_{n=0}^{N} \sum_{m=-n}^{n} b_n^m Y_n^m(\Theta,\Phi) \tag{18}$$

Also, let the measurements be represented as

$$m(\Theta,\Phi) = \sum_{n=0}^{N} \sum_{m=-n}^{n} a_n^m Y_n^m(\Theta,\Phi) \tag{19}$$

Substituting equations (18) and (19) into equation (15) and using equation (16) give

$$b_n^m = \frac{a_n^m}{\lambda_n}$$

and the radiant exitance estimate at the surface is

$$\hat{M}(\Theta,\Phi) = \sum_{n=0}^{N} \sum_{m=-n}^{n} \frac{a_n^m}{\lambda_n} Y_n^m(\Theta,\Phi) \tag{20}$$

Thus, the estimate of the radiant exitance depends on the coefficients of the measurement representation a_n^m and the eigenvalues of the measurement operator λ_n.

IMPLEMENTATION OF TECHNIQUES

Important to any data analysis technique is its application. Many times, ease of application dictates the choice of the technique. Such implementation details as the coordinate system, numerical techniques, computer time and storage requirements, and necessary assumptions are all part of a technique and affect the final results.

Field Representations

The radiant exitance field at the top of the Earth's atmosphere is represented in this paper in two ways: in a regional grid system and in a spherical harmonic system. Each system has advantages. The transformations from one representation to the other is necessary when comparing results.

The first system, illustrated in figure 2, is the basic regional grid system. It is obtained by dividing the Earth into 10° colatitude zones and then subdividing each zone into an even number of regions of equal area. The equatorial zones $80° \leq \Theta < 90°$ and $90° \leq \Theta < 100°$ each contain 36 regions, so that each region is bounded by 10° lines of colatitude and 10° lines of longitude. In all other zones, the number of regions is selected to make the areas of these regions as nearly as possible equal to those at the equator. All of these areas are referred to as either $10° \times 10°$ regions or simply 10° regions.

Three other regional grid systems are derived from this basic system. A 5° × 5° regional grid system is obtained by dividing each 10° region in half in both colatitude and longitude. A 2.5° × 2.5° regional grid system is obtained by dividing each 5° region in half in both colatitude and longitude. A third system is obtained by combining adjacent 10° regions in pairs in each zone to obtain 10° × 20° regions. The radiant exitance field is represented in these grid systems by a piecewise constant function over the regions.

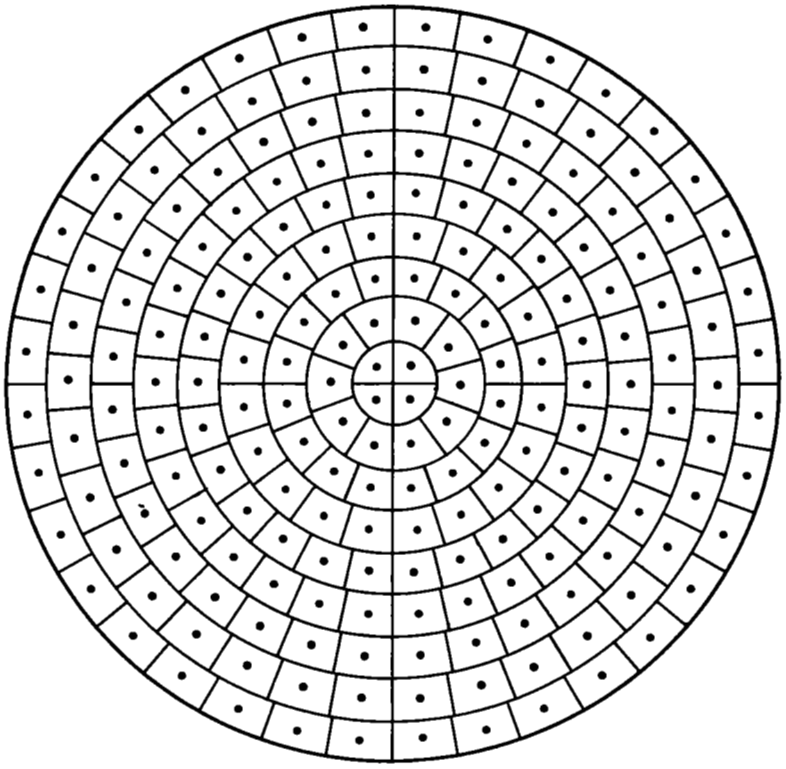

Figure 2.- Polar view of 10° × 10° regional grid representation.

Another way to represent the radiant exitance field is by a system of spherical harmonics. If $X(\Theta,\Phi)$ is a real function on the surface of a sphere, then a representation of $X(\Theta,\Phi)$ is

$$X(\Theta,\Phi) = \sum_{n=0}^{N} \sum_{m=0}^{n} \left[C_n^m Y_{cn}^m(\Theta,\Phi) + S_n^m Y_{sn}^m(\Theta,\Phi) \right] \tag{21}$$

where C_n^m and S_n^m are real coefficients of the spherical harmonics Y_{cn}^m and Y_{sn}^m, respectively. The spherical harmonics are defined by

$$\left.\begin{aligned} Y^m_{cn}(\Theta,\Phi) &= N^m_n \cos m\Phi\, P^m_n(\cos\Theta) \\ Y^m_{sn}(\Theta,\Phi) &= N^m_n \sin m\Phi\, P^m_n(\cos\Theta) \end{aligned}\right\} \tag{22}$$

where

$$N^m_n = \left[\frac{(2n+1)(n-m)!\left(2-\delta^m_0\right)}{(n+m)!}\right]^{1/2}$$

Moreover, the following properties apply:

$$\int_{\text{Sphere}} Y^m_{cn} Y^i_{cj}\, dA = \int_{\text{Sphere}} Y^m_{sn} Y^i_{sj}\, dA = 4\pi\delta^j_n \delta^i_m \tag{23}$$

$$\int_{\text{Sphere}} Y^m_{cn} Y^i_{sj}\, dA = 0 \tag{24}$$

where δ^m_n is the Kronecker delta function. The radiant exitance over the surface of the Earth can be defined by the coefficients C^m_n and S^m_n.

Transformation Between Regions and Spherical Harmonics

The regional grid system defines the radiant exitance at every point as a piecewise constant function in terms of the regional values. The spherical harmonic system defines the radiant exitance at every point as a linear combination of spherical harmonics in terms of the coefficients C^m_n and S^m_n. A given set of regional values can be transformed to spherical harmonic coefficients by the principle of orthogonal projection as follows. Multiplying equation (21) by $Y^i_{cj}(\Theta,\Phi)$, integrating over the sphere, and taking into account the orthogonality conditions of equations (23) and (24) give the coefficients as

$$C^m_n = \frac{1}{4\pi} \int_{\text{Sphere}} X(\Theta,\Phi)\, Y^m_{cn}(\Theta,\Phi)\, dA$$

Since $X(\Theta,\Phi)$ is known in terms of its regional values X_k, we have

$$C_n^m = \frac{1}{4\pi} \sum_{k=1}^{K} X_k \int_{\text{Region } k} Y_{cn}^m(\Theta,\Phi)\, dA$$

and from equation (22),

$$C_n^m = \frac{N_n^m}{4\pi} \sum_{k=1}^{K} X_k \int_{\Phi=\Phi_{k1}}^{\Phi_{k2}} \cos m\Phi\, d\Phi \int_{\Theta=\Theta_{k1}}^{\Theta_{k2}} P_n^m(\cos\Theta) \sin\Theta\, d\Theta$$

or

$$C_n^m = \frac{N_n^m}{4\pi} \sum_{k=1}^{K} X_k\, C_m(\Phi_{k1},\Phi_{k2})\, I_n^m(\Theta_{k1},\Theta_{k2}) \tag{25}$$

Similarly,

$$S_n^m = \frac{N_n^m}{4\pi} \sum_{k=1}^{K} X_k\, S_m(\Phi_{k1},\Phi_{k2})\, I_n^m(\Theta_{k1},\Theta_{k2}) \tag{26}$$

where subscripts 1 and 2 denote the boundaries of a region. The integrals in equations (25) and (26) are defined as

$$C_m(\Phi_1,\Phi_2) \equiv \int_{\Phi=\Phi_1}^{\Phi_2} \cos m\Phi\, d\Phi \tag{27}$$

$$S_m(\Phi_1,\Phi_2) \equiv \int_{\Phi=\Phi_1}^{\Phi_2} \sin m\Phi\, d\Phi \tag{28}$$

$$I_n^m(\Theta_1,\Theta_2) \equiv \int_{\Theta=\Theta_1}^{\Theta_2} P_n^m(\cos\Theta) \sin\Theta\, d\Theta \tag{29}$$

These quantities are efficiently computed by recursive formulas (Bess et al. 1981). Equations (25) and (26) define the transformation between the regional grid system and the spherical harmonic system.

The transformation from the spherical harmonic coefficients to the regional values also follows from the principle of orthogonal projection. The regional values of a function $X(\Theta,\Phi)$ are simply the average over the region, or

$$X_k = \frac{\int_{\text{Region } k} X(\Theta,\Phi)\, dA}{\int_{\text{Region } k} dA} = A_k^{-1} \int_{\Phi=\Phi_{k1}}^{\Phi_{k2}} \int_{\Theta=\Theta_{k1}}^{\Theta_{k2}} X(\Theta,\Phi) \sin\Theta \, d\Theta \, d\Phi \tag{30}$$

where A_k is the surface area of the kth region. Substituting for $X(\Theta,\Phi)$ and expressing the results in terms of definitions (27) through (29) yield

$$X_k = A_k^{-1} \sum_{n=0}^{N} \sum_{m=0}^{n} N_n^m I_n^m(\Theta_{k1},\Theta_{k2}) \left[C_n^m C_m(\Phi_{k1},\Phi_{k2}) + S_n^m S_m(\Phi_{k1},\Phi_{k2}) \right]$$

This equation defines the transformation from the spherical harmonic system to the regional grid system.

Relationship Between Region Size and Spherical Harmonic Representation

The transformation from the spherical harmonic system to the regional system is accomplished by averaging over the region (eq. (30)), which smooths the representation. Thus, the transformation from regional values back to spherical harmonic coefficients (eqs. (25) and (26)) yields a set of coefficients that represent the averaged or smoothed field. However, we wish to recapture as well as possible the original unsmoothed field from the regional values. Therefore, the spherical harmonic coefficients produced from this coordinate transformation must be increased, or enhanced, to represent the original field. Consider the smoothing parameter β_n defined by Pellinen (1967) and given by (appendix A)

$$\beta_n = \frac{1}{1 - \cos\gamma^*} \int_0^{\gamma^*} P_n^0(\cos\gamma) \sin\gamma \, d\gamma \tag{31}$$

If a field is smoothed by replacing each point value with the average value over a circular region with radius γ^*, then the coefficients $\tilde{C}_n^m$ and $\tilde{S}_n^m$ of the smoothed spherical harmonic representation are given by $\tilde{C}_n^m = \beta_n C_n^m$ and $\tilde{S}_n^m = \beta_n S_n^m$. Rapp (1977) has shown that smoothing over square regions can be approximated with β_n provided that an effective radius is used. The effective radius gives circular regions with the same surface area as square regions. For example, a $10° \times 10°$ region corresponds to a circular region with $\gamma^* = 5.63°$. The smoothing parameter

β_n is presented in figure 3 for two values of γ^*. Thus, to recapture the original spherical harmonic coefficients C_n^m and S_n^m from the regional values, we first calculate the spherical harmonic coefficients $\tilde{C}_n^m$ and $\tilde{S}_n^m$ that represent the smooth field (eqs. (25) and (26)) and then divide them by β_n, that is,

$$C_n^m = \beta_n^{-1}\tilde{C}_n^m \qquad S_n^m = \beta_n^{-1}\tilde{S}_n^m \tag{32}$$

This approach was followed throughout this study when spherical harmonics were computed from regional values.

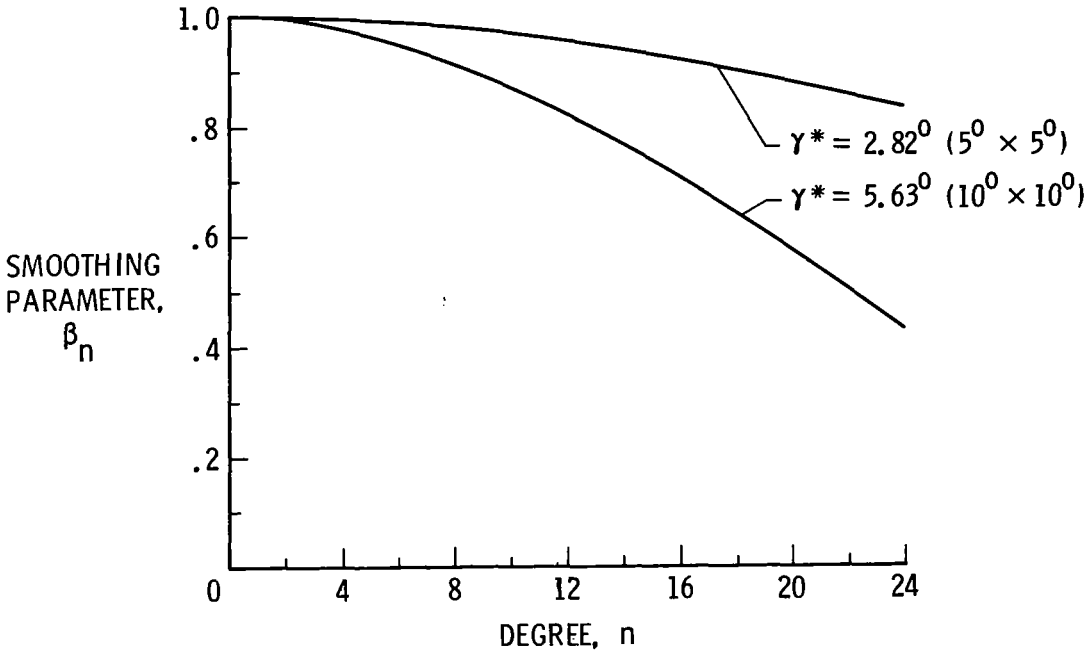

Figure 3.- Regional smoothing parameter.

Calculation of Important Parameters

A radiant exitance field can be characterized in a number of ways. Three important characteristic parameters are the zonal radiant exitance, the global radiant exitance, and the radiant exitance gradients. If the regional radiant exitance values are known, then the zonal radiant exitance $\hat{M}'_j$ is

$$\hat{M}'_j = \frac{\sum_i A_i \hat{M}_i}{\sum_i A_i} = \frac{1}{A'_j} \sum_i A_i \hat{M}_i \tag{33}$$

where i ranges over all regions in the jth colatitude zone and where the prime denotes zonal values. Similarly, the global radiant exitance is

$$\hat{M}_g = \frac{\sum_k A_k \hat{M}_k}{\sum_k A_k} = \frac{1}{A_g} \sum_k A_k \hat{M}_k \tag{34}$$

where A_g is the area of the globe and k ranges over all regions. It can be shown that the global radiant exitance is identical to C_0^0 as given by equation (25). In addition, we define the pole-to-pole gradient as C_1^0 and the equator-to-pole gradient as C_2^0. The deconvolution technique produces these values directly since they are spherical harmonic coefficients, whereas the shape factor and parameter estimation techniques produce regional values from which the gradient values are determined by equation (25).

The radiation fields produced by the three analysis techniques are compared in two ways. The first comparison is in physical space by comparing regional values, and the second comparison is in spectral space by comparing the spherical harmonic coefficients.

Comparison in physical space.- Define the difference in the ith 10° region between two radiation fields as ΔM_i. The differences $\Delta M_j'$ in the zonal radiant exitances follow from equation (33) with M_i replaced by ΔM_i. Further, we define the average zonal difference as

$$\left.\begin{array}{l}\text{Area weighted mean}\\ \text{of absolute zonal}\\ \text{difference}\end{array}\right\} = A_g^{-1} \sum_{j=1}^{18} A_j' |\Delta M_j'| \tag{35}$$

We also define the average 10° regional difference as

$$\left.\begin{array}{l}\text{Area weighted mean}\\ \text{of absolute 10°}\\ \text{regional difference}\end{array}\right\} = A_g^{-1} \sum_{k=1}^{K} A_k |\Delta M_k| \tag{36}$$

Another descriptive parameter is

$$\left.\begin{array}{l}\text{Standard deviation of}\\ \text{regional differences}\end{array}\right\} = \left[A_g^{-1} \sum_{k=1}^{K} A_k (\Delta M_k - \overline{\Delta M})^2\right]^{1/2} \tag{37}$$

where

$$\overline{\Delta M} = A_g^{-1} \sum_{k=1}^{K} A_k (\Delta M_k)$$

We can also calculate the correlation coefficient between field 1 and field 2 on a 10° regional scale as

$$\rho = \frac{A_g^{-1} \sum_{k=1}^{K} A_k (M_{1k} - \bar{M}_1)(M_{2k} - \bar{M}_2)}{\left[A_g^{-1} \sum_{k=1}^{K} A_k (M_{1k} - \bar{M}_1)^2\right]^{1/2} \left[A_g^{-1} \sum_{k=1}^{K} A_k (M_{2k} - \bar{M}_2)^2\right]^{1/2}} \tag{38}$$

where

$$\bar{M} = A_g^{-1} \sum_{k=1}^{K} A_k M_k .$$

Comparison in spectral space.- In spectral space, we compare the degree dispersions σ_n of each field given by

$$\sigma_n = \left\{ \sum_{m=0}^{n} \left[\left(C_n^m\right)^2 + \left(S_n^m\right)^2 \right] \right\}^{1/2} \qquad (n = 1, 2, \ldots, N) \tag{39}$$

APPLICATION OF TECHNIQUES TO DATA SET

The three techniques which have been presented were used to analyze wide field of view radiometer data to produce a radiant exitance field at the top of the atmosphere. Each technique has its own assumptions and limitations which are examined individually in this section. The same data set was used for all numerical examples, so that the differences in the derived radiation fields are entirely due to the technique and the assumptions employed.

Earth Radiation Data

The measurement data used in this study to define the Earth's longwave radiation field were obtained from the Earth Radiation Budget (ERB) instrument aboard the Nimbus 6 satellite. A description of the ERB instrument and calibration is given by Smith et al. (1977). The data tapes were supplied by the National Oceanic and Atmospheric Administration.

The ERB instrument obtained both fixed wide-angle and scanning narrow-angle measurements. The data considered here are the fixed wide-angle measurements at satellite altitude. One data channel recorded the total Earth measurement (0.2 to 50 μm) and another channel recorded the shortwave measurement (0.2 to 3.8 μm). The longwave contribution is the difference between these two measurements. The ERB instrument operated with a duty cycle of 2 days on and 2 days off. Measurements were taken every 16 seconds. The data set for this study consists of approximately 46 000 wide-angle measurements taken during August 1975. The emphasis in this study is not on the measurement data or the derived fields but on the differences in the fields derived with different assumptions and techniques.

The model of the radiant exitance field is independent of time; thus all measurement data were collected into 5° × 5° regions at satellite altitude (h = 1070 km) and averaged. We processed only 1664 averages instead of the 46 000 individual measurements.

Shape Factor Technique

With the shape factor technique, the radiant exitance at the top of the atmosphere is derived from each measurement by dividing by a shape factor (eq. (6)). The two basic assumptions are that (1) the radiant exitance at the top of the atmosphere is constant over the field of view and (2) the estimate of radiant exitance is associated with the region which contains the nadir point. As a result of the first assumption, which is a great simplification, the technique yields point estimates of the radiant exitance at nadir that are about 5 percent in error (Weaver and Green 1980, Green 1981). However, these estimates are seldom interpreted as point estimates but are used to represent the average radiant exitance over an area. In fact, these estimates best represent the average radiant exitance over a circular surface area centered at nadir with a 20° diameter. On the average with the shape factor technique, the average radiant exitance over this area can be estimated to within about 1 percent (Weaver and Green 1980, Green 1981). In this study we do not consider point estimates or estimates over circular regions, but estimates over square regions, over zones, and over the globe. All estimates of radiant exitance whose nadir points are in a particular area are averaged. Thus, the assumption of constant radiant exitance over the field of view is not as restrictive as one might imagine. The larger the area, the more appropriate the assumption. The second assumption of associating the estimate of radiant exitance with the region that contains the nadir point follows from the geometry of the measurement. For a uniform field, an incremental area centered at nadir has more influence on the measurement than any other incremental area in the field of view.

In addition to these two assumptions, two simplifying assumptions have been made about the directional function. First, we assume that $R(\theta)$ is the same for all points on the globe. This assumption was shown to yield a shape factor which is independent of the directional function, namely, $F = [R_e/(R_e + h)]^2$. Second, we model h as a constant, 1070 km for the Nimbus 6 data set. Thus, for an Earth radius of 6378 km and an atmospheric height of 30 km, we have a shape factor of

$$F = \left(\frac{6378 + 30}{6378 + 30 + 1070}\right)^2 = 0.7343 \tag{40}$$

With these assumptions the only parameter that affects the derived radiation field is the size of the regional grid system that is employed. The 46 000 measurements have been averaged over a 5° × 5° grid system at satellite altitude. Each of these averages is divided by the shape factor to produce an estimate of the average radiant exitance of a 5° × 5° region at the top of the atmosphere. These estimates can easily be combined to yield 10° × 10° regional radiant exitance estimates. Another approach would be to average the 46 000 measurements over a 10° × 10° grid system at satellite altitude and then to reduce each average to the top of the atmosphere. This approach allows for less spatial variation and can be considered inferior to the first approach. The difference between these two solutions illustrates the effect of the grid system size.

Table I presents these two solutions and the differences between them. The global radiant exitances as given by equation (34) differ by 0.30 $W\text{-}m^{-2}$ because of

TABLE I.- SOLUTIONS FROM SHAPE FACTOR TECHNIQUE ILLUSTRATING EFFECT OF GRID SYSTEM

Parameter	Case 1, data averaged over 5° regions	Case 2, data averaged over 10° regions	Case 1 minus case 2
Global radiant exitance, $W\text{-}m^{-2}$	235.39	235.09	0.30
Pole-to-pole gradient, $W\text{-}m^{-2}$	11.40	11.61	-.21
Equator-to-pole gradient, $W\text{-}m^{-2}$	-22.03	-22.27	.24
10° regional radiant exitance, $W\text{-}m^{-2}$:			
Pacific, tropical	266.03	265.58	.45
Pacific, high latitude	191.33	191.23	.10
Atlantic, subtropical	268.29	268.02	.27
Sahara	279.59	281.60	-2.01
Greenland	221.09	220.71	.38
South Pole	124.50	118.57	5.93
Area weighted mean of absolute zonal differences, $W\text{-}m^{-2}$			0.34
Area weighted mean of absolute 10° regional differences, $W\text{-}m^{-2}$			.83
Standard deviation of 10° regional differences, $W\text{-}m^{-2}$			1.44

the grid system. The pole-to-pole gradient and the equator-to-pole gradient are given by the spherical harmonic coefficients C_1^0 and C_2^0, respectively, at the top of the atmosphere, as determined from equations (25) and (32). The global value C_0^0 can also be calculated from these equations which give the same value as equation (34), since the smoothing is given by $\beta_0 = 1$. Also included in table I are the 10° regional radiant exitances for six specific regions. The average zonal difference as computed from equation (35) is 0.34 $W\text{-}m^{-2}$, nearly the same as the global difference of 0.30 $W\text{-}m^{-2}$. In general, the smaller the area in question, the greater the difference. This is illustrated by the average regional difference of 0.83 $W\text{-}m^{-2}$ as computed from equation (36) and their standard deviation of 1.44 $W\text{-}m^{-2}$ from equation (37). If we consider the range of regional differences to be $\pm 2\sigma$ about their

mean, then they range over 0.30 ± 2 (1.44), or from -2.58 $W\text{-}m^{-2}$ to 3.18 $W\text{-}m^{-2}$. (The mean regional difference is given by the global difference (0.30 $W\text{-}m^{-2}$).) The six specific regional differences all fall within this range of differences except for the South Pole.

The zonal differences for the two solutions are plotted in figure 4. Notice the unusually large difference for $160° \leq \Theta \leq 170°$ compared with the small differences for all other zones. The problem is due to nonuniform satellite sampling combined with a large latitudinal gradient. Using the 5° grid system, we can determine the 5° zonal radiant exitance from $160° \leq \Theta \leq 165°$ to be 145.38 $W\text{-}m^{2}$ and from $165° \leq \Theta \leq 170°$ to be 123.35 $W\text{-}m^{-2}$. By averaging the two 5° zonal radiant exitances with the appropriate area weighting, we obtain 136.16 $W\text{-}m^{-2}$ which corresponds to the 5° grid system solution. In the 10° grid system, this 5° zonal distinction is not made; averaging all data between $160° \leq \Theta \leq 170°$ results in 129.54 $W\text{-}m^{-2}$. If the

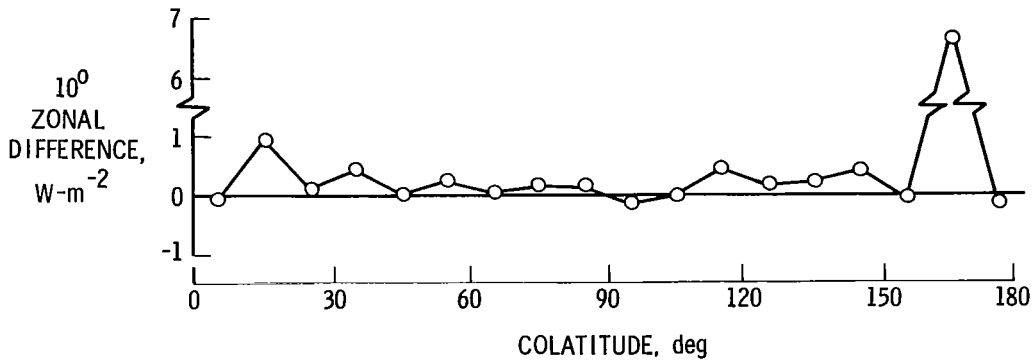

Figure 4.- Zonal differences due to grid system (5° or 10°) for shape factor technique.

satellite sample were uniform with area, then the 10° zonal results would be the same. Since the number of measurements for $160° \leq \Theta \leq 165°$ was 841 and the number of measurements for $165° \leq \Theta \leq 170°$ was 2154, the southern zone was weighted more. This nonuniform sampling is a result of orbital geometry and data elimination due to Sun contamination (Bess et al. 1981). The difference in the $160° \leq \Theta \leq 170°$ zonal radiant exitance is also a function of the latitudinal gradient. If the 5° zonal values were equal, then the number of measurements would not matter. Notice that the difference in the $10° \leq \Theta \leq 20°$ zonal radiant exitance is not nearly as large. This results from a smaller latitudinal gradient for the northern zone. Nonuniform sampling combined with a large latitudinal gradient is also the cause of the large difference in radiant exitance for the South Pole 10° region.

The question arises as to why large differences in radiant exitance do not occur for the $170° \leq \Theta \leq 180°$ zone. The Nimbus 6 orbit has an inclination slightly less than 100°, which means that the nadir point slightly exceeds a latitude of ±80°. Thus, we have sampling for the $170° \leq \Theta \leq 180°$ zone, although all of it is near $\Theta = 170°$. A similar situation exists at the North Pole. For the 5° grid system, the satellite samples $170° \leq \Theta \leq 175°$ but not $175° \leq \Theta \leq 180°$. Thus, we must extrapolate into the $175° \leq \Theta \leq 180°$ zone. The rule has been adopted to set this zonal radiant exitance equal to the $170° \leq \Theta \leq 175°$ estimate. Since both 5° zones have the same radiant exitance, we understandably obtain an estimate for the 5° grid system which is similar to the 10° grid system estimate.

If reducing the size of the grid system from a 10° grid to a 5° grid changes the $160° \leq \Theta \leq 170°$ zonal estimate, then what effect does further reducing the grid system to 2.5° have? The 5° grid, like the 10° grid, overweights the estimates toward the polar values because of the satellite sampling. The 2.5° grid reduces this bias and increases the zonal radiant exitance to 137.92 $W\text{-}m^{-2}$ for $160° \leq \Theta \leq 170°$. However, this small change may not be significant compared with the accuracy of the shape factor technique.

Parameter Estimation Technique

With the parameter estimation technique, all measurements are processed together as a batch and the radiant exitance estimate at the top of the atmosphere is a least squares fit to the data using equation (14). The two basic assumptions are that (1) the radiant exitance at the top of the atmosphere is constant over a region and (2) the directional function is known for each region. The first assumption is reasonable since we desire to estimate the mean radiant exitance over a region, and the estimates we obtain by assuming the radiant exitance to be constant closely resemble the mean regional radiant exitances. The second assumption of known directional functions introduces errors into the estimates. Estimates of the radiant exitance for large areas like the globe or a zone are not as sensitive to the directional functions as regional estimates. These errors are examined in this section by a numerical example.

One problem with implementing the parameter estimation technique (eq. (14)) is the size of the B^TB matrix. There are 416, 10° × 10° regions over the globe. Thus, the 416 × 416 B^TB matrix contains 173 056 elements or 83 736 if symmetry is taken into account. The required computer storage was reduced by one-fourth by estimating the radiant exitance in 10° × 20° regions. These 10° × 20° estimates are divided into 10° × 10° estimates by a curve fitting scheme presented in appendix B.

A source of error is the choice of the directional function for the 208 rectangular 10° × 20° regions. This function has been denoted $R_k(\theta)$ and is included in the calculation of B_{ik} (eq. (12)). The effect of different functions was examined by two numerical examples in which all 10° × 20° regions were assumed to have the same directional function. In the first case the radiation was assumed to be Lambertian, or $R_k(\theta) = 1$. In the second case a directional function with a considerable amount of limb darkening was assumed and is given by

$$R(\theta) = 1.106 \exp\left(0.0547(1 - \sec\theta) + 0.09375\{\exp[2.24(1 - \sec\theta)] - 1\}\right) \qquad (41)$$

where $0° \leq \theta \leq 90°$. This function represents a lower bound to a family of limb darkening functions based on Nimbus 2 data (Raschke et al. 1973). If these two directional functions are considered upper and lower bounds, the two solutions establish bounds on the radiant exitance due to uncertainty in the regional directional functions.

Part of the implementation of the parameter estimation technique is the selection of a quadrature formula of the influence coefficients given by equation (12), that is,

$$B_{ik} = \frac{1}{\pi} \int_{FOV_{ik}} R_k(\theta_i) \cos \alpha_i \frac{\cos \theta_i}{r_i^2} dA$$

where B_{ik} is the influence of the kth region (10° × 20° region) on the ith measurement, and the integration is over the ith field of view that is also in the kth region. A very practical numerical integration scheme is to subdivide the regional grid system into smaller subregions and approximate the integral of equation (12) by

$$B_{ik} = \frac{1}{\pi} \sum_j R_k(\theta_{ij}) \cos \alpha_{ij} \frac{\cos \theta_{ij}}{r_{ij}^2} A_j \qquad (42)$$

where j ranges over all the subregions that are in both the ith field of view and the kth region. The subscript j denotes that a parameter is evaluated at the center point of the jth subregion. Also, a subregion is included in the summation if its center point qualifies and is excluded otherwise. This means that the boundaries of the integration are approximated by meridional and latitudinal lines. This boundary error and the quadrature error are reduced by making the subgrid system smaller at the expense of computational effort. Numerical examples are given for two different subgrid systems.

Three numerical examples are presented in table II. The measurement data for each example are the same and were averaged into 5° × 5° regions at satellite altitude. This reduced the number of measurements to 1664 values, which were processed

TABLE II.- SOLUTIONS FROM PARAMETER ESTIMATION TECHNIQUE ILLUSTRATING EFFECTS OF QUADRATURE SUBGRID SYSTEM AND DIRECTIONAL FUNCTION

Parameter	Case 1, Lambertian R, 5° quadrature	Case 2, Lambertian R, 2.5° quadrature	Case 3, limb darkening R, 2.5° quadrature	Case 1 minus case 2	Case 2 minus case 3
Global radiant exitance, $W\text{-}m^{-2}$	235.37	235.42	235.42	-0.05	0
Pole-to-pole gradient, $W\text{-}m^{-2}$	11.59	11.61	11.58	-.02	.03
Equator-to-pole gradient, $W\text{-}m^{-2}$	-23.44	-23.35	-23.21	-.09	-.14
10° regional radiant exitance, $W\text{-}m^{-2}$:					
Pacific, tropical	270.72	270.64	270.73	.08	-.09
Pacific, high latitude	187.63	186.87	187.72	.76	-.85
Atlantic, subtropical	279.65	280.04	278.91	-.39	1.13
Sahara	307.34	308.38	305.45	-1.04	2.93
Greenland	225.30	226.29	225.59	-.99	.70
South Pole	97.98	96.55	99.71	1.43	-3.16
Computer time, sec	120	335	456		
Area weighted mean of absolute zonal differences, $W\text{-}m^{-2}$				0.56	0.85
Area weighted mean of absolute 10° regional differences, $W\text{-}m^{-2}$				.76	1.20
Standard deviation of 10° regional differences, $W\text{-}m^{-2}$				1.09	1.51

with the parameter estimation technique (eq. (14)). In the first two cases, we assumed the radiation to be Lambertian and used a 5° and a 2.5° subgrid quadrature scheme. The average zonal difference is 0.56 $W\text{-}m^{-2}$ and the average regional difference is 0.76 $W\text{-}m^{-2}$. Since the global difference is approximately zero (-0.05 $W\text{-}m^{-2}$), the average zonal and regional differences reflect the true differences in the shape of the radiant exitance field. It is reasonable to expect the 2.5° subgrid quadrature scheme to give the better results since the quadrature errors are smaller. The computer time, also listed in the table, is about three times greater for the smaller subgrid quadrature. However, 335 seconds of computer time on a Control Data CYBER 173 computer is not considered excessive, so that a 2.5° quadrature scheme was adopted for this study. The zonal differences are plotted in figure 5 and are relatively small except for the northern and southern zones.

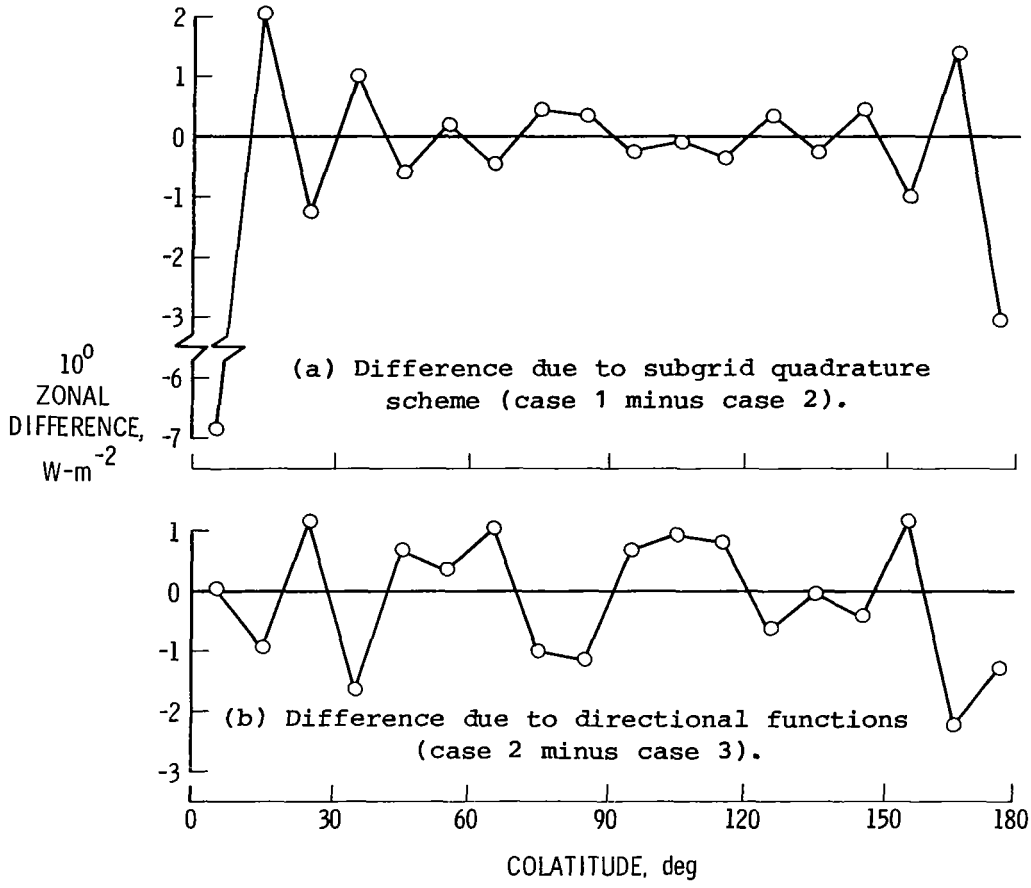

Figure 5.- Zonal differences for parameter estimation technique.

Cases 2 and 3 in table II represent the differences due to different directional functions. The differences are very small on a global scale, larger on a zonal scale, and still larger on a regional scale. The global radiant exitance was the same for both cases, and the average zonal difference was 0.85 $W\text{-}m^{-2}$. The average regional difference was 1.20 $W\text{-}m^{-2}$, and we would expect the individual regional differences to range between ± 3.02 $W\text{-}m^{-2}$. Also, assuming a limb darkening function increases the computer time from 335 to 456 seconds. It is not clear which of these two solutions best represents the true radiant exitance field. The first assumes no limb darkening, while the second probably overestimates the limb darkening. Assuming

a limb darkening function between these two would probably give better results. Moreover, if the directional character of each region were known then the solution would be improved even further. The purpose here, however, is to define on a global, zonal, and regional scale the differences due to the extreme directional functions.

Deconvolution Technique

With the deconvolution technique, we take advantage of the fact that spherical harmonics are the eigenfunctions of the measurement operator. If the measurements are used to define the radiant exitance field at satellite altitude in terms of a spherical harmonic expansion, then the field is easily reduced to the top of the atmosphere by the eigenvalues (eq. (20)). This solution is based on the following three simplifying assumptions: (1) the sensor integrates incoming radiation over its field of view with its directional response $S(\alpha)$ being a function only of the nadir angle, (2) the directional dependence of exiting radiation at each point of the top of the atmosphere is a function only of the zenith angle of the exiting ray, and (3) continuous measurements are available over a sphere concentric with the Earth.

The first assumption is applicable to most wide field of view sensors because of their design. Throughout this study we have used $S(\alpha) = \cos \alpha$, or a flat-plate sensor model. The second assumption, which states that $R(\Theta,\Phi,\theta) = R(\theta)$, is a reasonable approximation for Earth emitted radiation. The third assumption contains two requirements. The first is that the measurements be continuous over a sphere. Since physical systems provide discrete measurements, we calculate the spherical harmonic coefficients with equations (25) and (26) and then approximate the continuous case with the smoothing parameter β_n. The second requirement is that the orbit be circular.

The implementation of the deconvolution technique requires that we define the directional function $R(\theta)$ and that we truncate the spherical harmonic expansion at some finite degree. To investigate the dependence of the solution on the directional function, the limiting cases of a Lambertian function ($R(\theta) = 1$) and a limb darkening function (eq. (41)) have been examined. These directional functions affect the solution through the eigenvalues (eq. (17)), which are given in table III for degree 0 through degree 12. Note that $\lambda_0 = 0.7343$ for both directional functions; thus, the

TABLE III.- EIGENVALUES OF MEASUREMENT OPERATOR

[R_e = 6378 + 30 = 6408 km; h = 1070 km]

Degree, n	λ_n for -	
	Lambertian R	Limb darkening R
0	0.7343	0.7343
1	.7217	.7233
2	.6975	.7019
3	.6632	.6713
4	.6208	.6331
5	.5726	.5893
6	.5214	.5419
7	.4693	.4929
8	.4185	.4443
9	.3707	.3974
10	.3267	.3535
11	.2874	.3132
12	.2526	.2770

global radiant exitance is unaffected by directional function. It is also interesting that λ_0 is the shape factor (eq. (40)) used in the shape factor technique. To examine the effect of the degree of truncation on the solution, we have expanded the measurements at satellite altitude in a series of spherical harmonics to degree 24 by equations (25) and (26) and approximated the continuous solution by using β_n based on 5° × 5° regions. The degree dispersion (eq. (39)) for this solution is given in figure 6. The radiant exitance estimate at the top of the atmosphere was computed

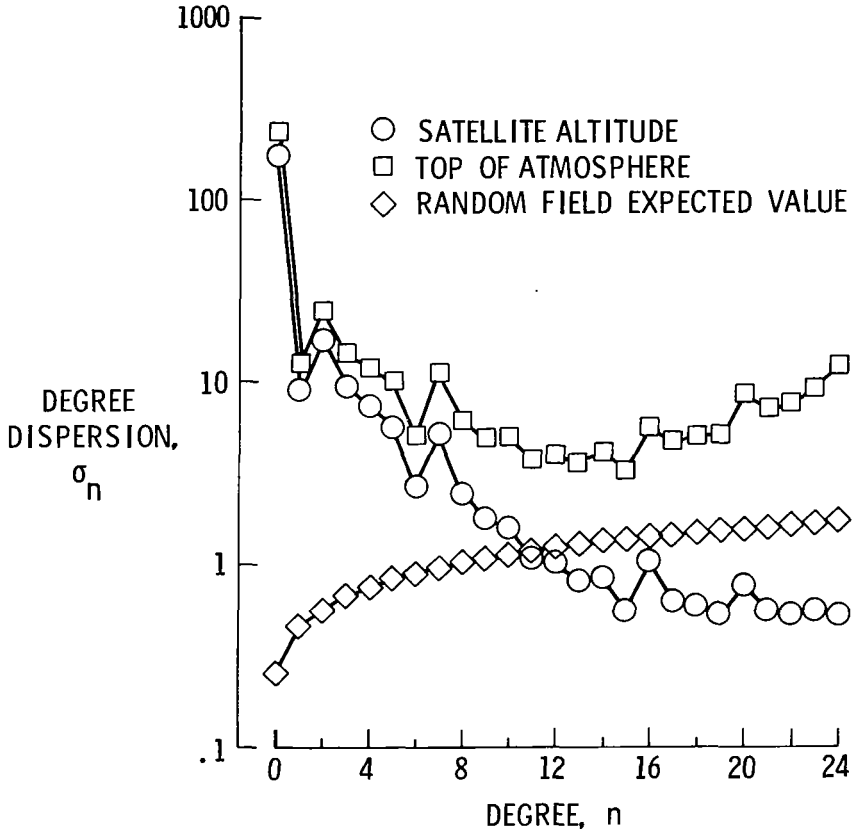

Figure 6.- Degree dispersion of deconvolution solution based on Lambertian directional function.

by dividing the spherical harmonic coefficients by the eigenvalues λ_n based on Lambertian radiation. The divergence of these two solutions in figure 6 is due to the smoothing effect of the measurement operator. It is seen that the radiant exitance spectrum measured at satellite altitude can be divided into two regions, one in which $\log \sigma_n$ decreases approximately linearly with n for $n \leq 15$, and one in which $\log \sigma_n$ is rather constant for $n > 15$. The spectrum at the top of the atmosphere likewise consists of two regions, one in which $\log \sigma_n$ decreases somewhat linearly for $n \leq 15$, and one in which $\log \sigma_n$ increases somewhat linearly for $n > 15$. The nearly constant spectrum at satellite altitude is interpreted as measurement noise and produces the divergence of the solution at the top of the atmosphere since the eigenvalues are a decreasing sequence of values. Thus, it is

concluded from figure 6 that the coefficients for $n > 15$ are due primarily to noise and contain little information concerning the radiant exitance field; the expansion is therefore truncated at $N = 15$.

The interpretation of a nearly constant spectrum as random noise is illustrated by examining the spectrum of a random field. This field is defined on a 5° regional grid system where each regional value is a normal random variable with mean of zero and standard deviation of 10 $W\text{-}m^{-2}$. The expected value of the spectrum for this field is derived in appendix C and presented in figure 6. Although this spectrum for a random field gradually increases for $n > 15$, it gives support to the interpretation of a nearly constant spectrum as noise.

To investigate the sensitivity of the solution to the directional functions and the degree of truncation, three cases were examined, as given in table IV. Two limiting directional functions were examined and two different truncation degrees.

TABLE IV.- SOLUTIONS FROM DECONVOLUTION TECHNIQUE ILLUSTRATING DEGREE OF TRUNCATION AND OF DIRECTIONAL FUNCTION

Parameter	Case 1, Lambertian R, degree 15	Case 2, Lambertian R, degree 12	Case 3, limb darkening R, degree 12	Case 1 minus case 2	Case 2 minus case 3
Global radiant exitance, $W\text{-}m^{-2}$	235.39	235.39	235.39	0	0
Pole-to-pole gradient, $W\text{-}m^{-2}$	11.60	11.60	11.58	0	.02
Equator-to-pole gradient, $W\text{-}m^{-2}$	-23.19	-23.19	-23.05	0	-.14
10° regional radiant exitance, $W\text{-}m^{-2}$:					
Pacific, tropical	259.70	263.94	264.26	-4.24	-.32
Pacific, high latitude	190.99	191.40	191.65	-.41	-.25
Atlantic, subtropical	281.28	274.47	273.52	6.81	.95
Sahara	283.54	289.95	288.46	-6.41	1.49
Greenland	215.67	213.77	214.32	1.90	-.55
South Pole	109.38	111.05	113.15	-1.67	-2.10
Area weighted mean of absolute zonal differences, $W\text{-}m^{-2}$				0.85	0.55
Area weighted mean of absolute 10° regional differences, $W\text{-}m^{-2}$				3.94	.75
Standard deviation of 10° regional differences, $W\text{-}m^{-2}$				4.89	.94

As discussed previously, a reasonable choice of the degree of truncation is $N = 15$ based on the present 1-month data set. However, Bess et al. (1981) have investigated 12 months of Nimbus 6 data and concluded that $N = 12$ is the appropriate expansion limit. Therefore, the two solutions based on $N = 12$ and 15 are compared in table IV. This comparison reveals that the average regional difference due to truncation is 3.94 $W\text{-}m^{-2}$. Also, the average regional difference due to different directional functions is 0.75 $W\text{-}m^{-2}$. Thus, we conclude that on a regional scale, the degree of truncation has more influence on the solution than the directional function. The effect of truncation is reduced, however, on a zonal scale, since the addition of the high-frequency coefficients ($n = 13, 14, 15$) does not affect the

zonal values as much as the regional values. The average zonal difference due to truncation is 0.85 $W\text{-}m^{-2}$ and due to different directional functions is 0.55 $W\text{-}m^{-2}$. The individual zonal differences are plotted in figure 7. The degree at which the spherical harmonic expansion should be truncated is very important to the analysis. However, there is not a clear criterion for choosing this degree. For the remainder of this study we use a spherical harmonic expansion to degree 12 for the deconvolution technique.

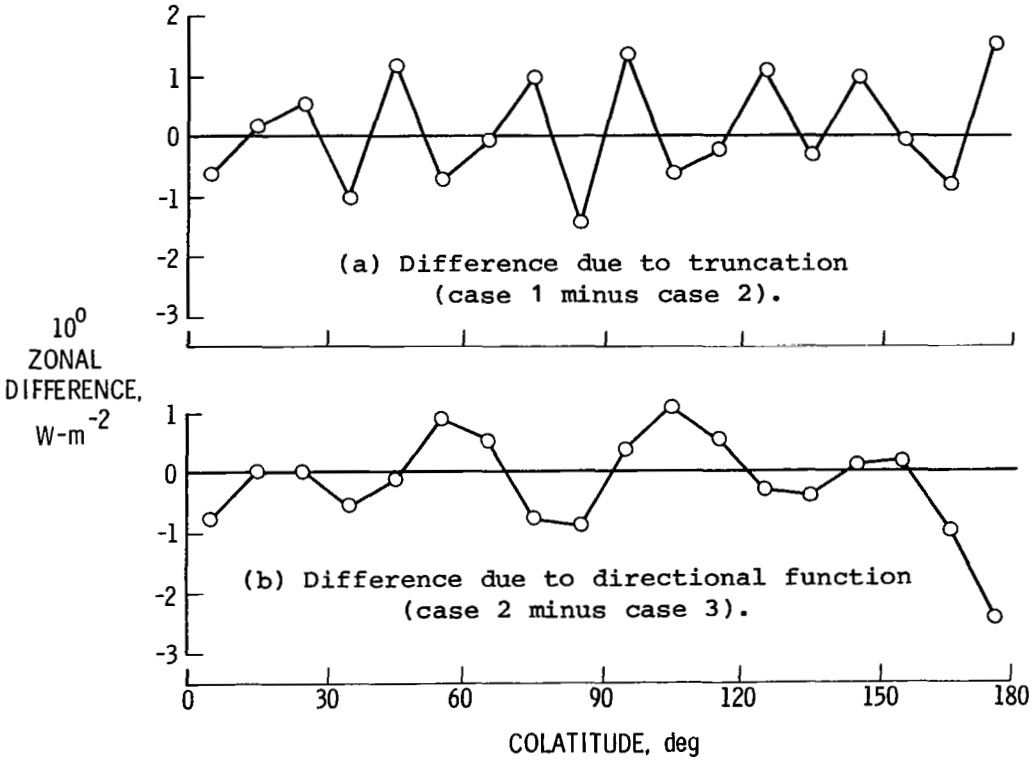

Figure 7.- Zonal differences for deconvolution technique.

COMPARISON OF TECHNIQUES

The three data analysis techniques have been derived and examined individually to establish their necessary assumptions and characteristics. In this section, these techniques are compared numerically. Since each technique processes the same measurement data, any differences in the derived radiation fields are a result of the techniques themselves.

A summary of the three radiation fields that result from the three techniques is presented in table V and the zonal differences are plotted in figure 8. The shape factor solution corresponds to the 5° regional grid system and was presented in table I. This case was chosen to represent the shape factor technique so that all techniques would have not only a common data set but also a common grid system. The parameter estimation solution corresponds to the Lambertian directional function and

TABLE V.- SOLUTIONS FROM THREE TECHNIQUES FOR COMPARISON

Parameter	Shape factor	Parameter estimation	Deconvolution	Shape factor minus parameter estimation	Shape factor minus deconvolution	Parameter estimation minus deconvolution
Global radiant exitance, $W\text{-}m^{-2}$	235.39	235.42	235.39	-0.03	0	0.03
Pole-to-pole gradient, $W\text{-}m^{-2}$	11.40	11.61	11.60	-.21	-.20	.01
Equator-to-pole gradient, $W\text{-}m^{-2}$	-22.03	-23.35	-23.19	1.32	1.16	-.16
10° regional radiant exitance, $W\text{-}m^{-2}$:						
Pacific, tropical	266.03	270.64	263.94	-4.61	2.09	6.70
Pacific, high latitude	191.33	186.87	191.40	4.46	-.07	-4.53
Atlantic, subtropical	268.29	280.04	274.47	-11.75	-6.18	5.57
Sahara	279.59	308.38	289.95	-28.79	-10.36	18.43
Greenland	221.09	226.29	213.77	-5.20	7.32	12.52
South Pole	124.50	96.55	111.05	27.95	13.45	-14.50
Area weighted mean of absolute zonal differences, $W\text{-}m^{-2}$				7.42	4.04	4.84
Area weighted mean of absolute 10° regional differences, $W\text{-}m^{-2}$				10.65	5.95	8.60
Standard deviation of 10° regional differences, $W\text{-}m^{-2}$				13.51	7.44	10.78
Correlation (regional scale)				.95	.98	.97

a 2.5° quadrature scheme and was first presented in table II. The Lambertian function was chosen for its simplicity, and the 2.5° quadrature scheme for its accuracy. The deconvolution solution taken from table IV corresponds to a spherical harmonic expansion to degree 12 and a Lambertian directional function. The 12th degree expansion was chosen since it probably represents the appropriate expansion limit for monthly information over a yearly cycle, as discussed by Bess et al. (1981). The Lambertian function was chosen so that the parameter estimation and the deconvolution would have no differences due to the directional function. All three techniques produced essentially the same estimate of the global radiant exitance. This is characteristic of a flat-plate sensor and the wide field of view measurement. The other pertinent parameters, however, depend on the technique employed.

The differences in these three solutions also are presented in table V. The two solutions that correlate best on a 10° regional scale (eq. (38)) are the shape factor and the deconvolution solutions, their correlation being 0.98. Their average zonal difference is 4.04 $W\text{-}m^{-2}$ and their average regional difference is 5.95 $W\text{-}m^{-2}$. It is surprising that the two techniques with the highest correlation should vary by this large amount. The regional standard deviation of 7.44 $W\text{-}m^{-2}$ implies that about 95 percent of the regional differences are between ± 15 $W\text{-}m^{-2}$. The two solutions with the least correlation are the shape factor and the parameter estimation solutions.

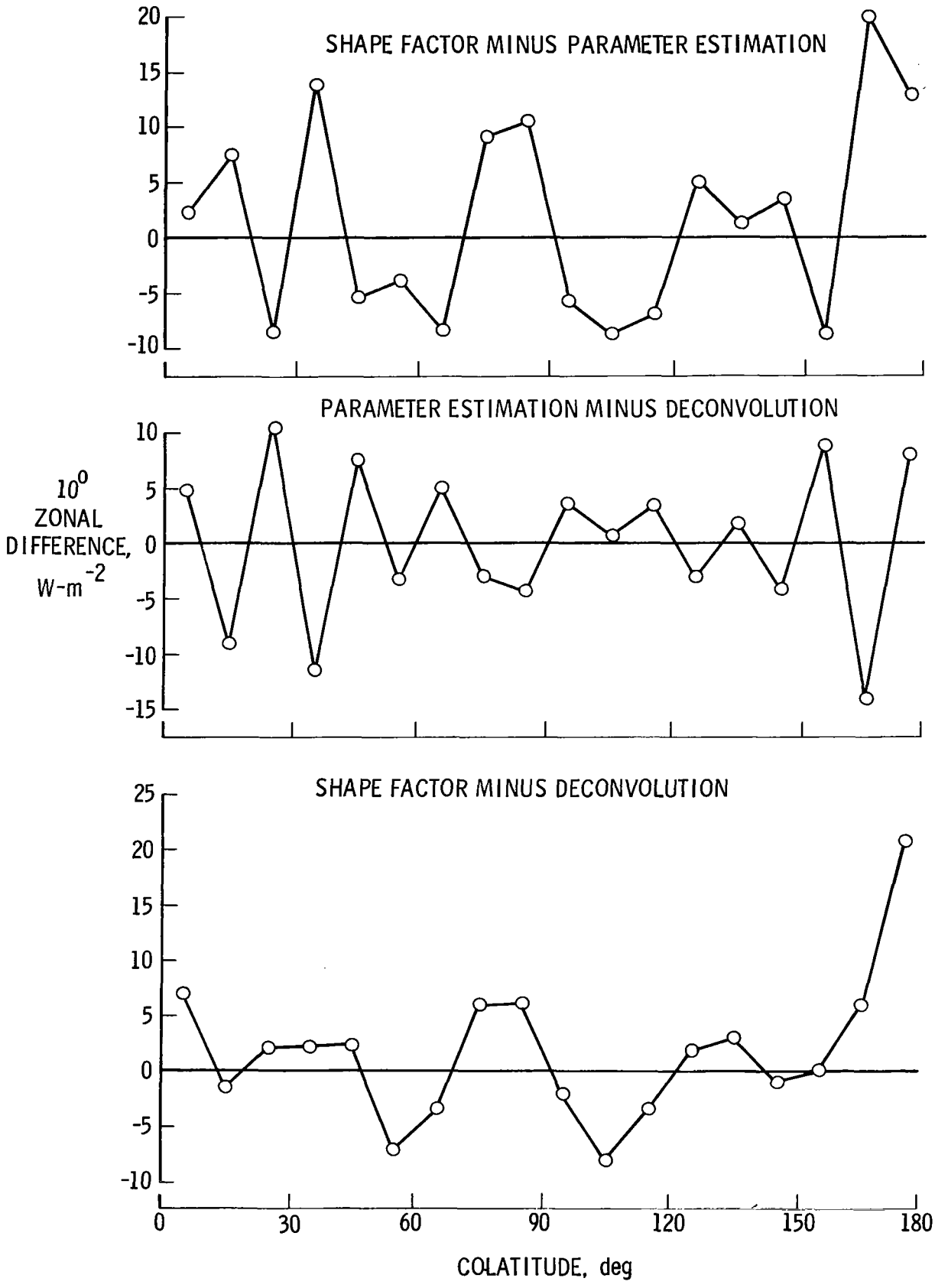

Figure 8.- Zonal differences for three techniques.

The regional standard deviation for these two solutions was 13.51 $W\text{-}m^{-2}$. The distributions of these differences are presented in histograms in figure 9. These distributions are approximately normal and centered about zero. The common global value

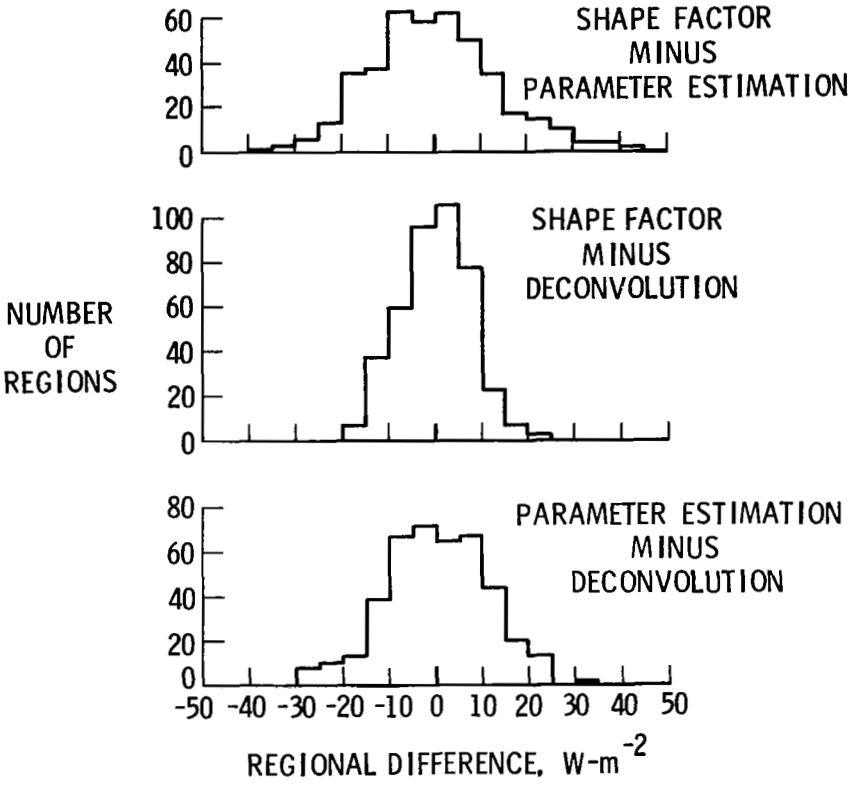

Figure 9.- Histograms of regional differences for the three techniques.

for the three solutions results in the zero means. Again, we see that the shape factor and the deconvolution solutions are most similar on a regional scale.

The three solutions can also be compared by examining their spatial spectra. The basic representation of the deconvolution solution is in the spherical harmonic coordinate system. The shape factor and the parameter estimation solutions have been transformed to the spherical harmonic system, and the spatial spectrums of all three solutions are compared in figure 10. The spectrum of the parameter estimation solution decreases up to about degree 15 and then exhibits a different type of behavior. The deconvolution spectrum follows the parameter estimation spectrum very closely to degree 12 and is zero from there on because of the 12th degree truncation. The shape factor spectrum gradually departs from the other two spectrums, the departure becoming significant after degree 3.

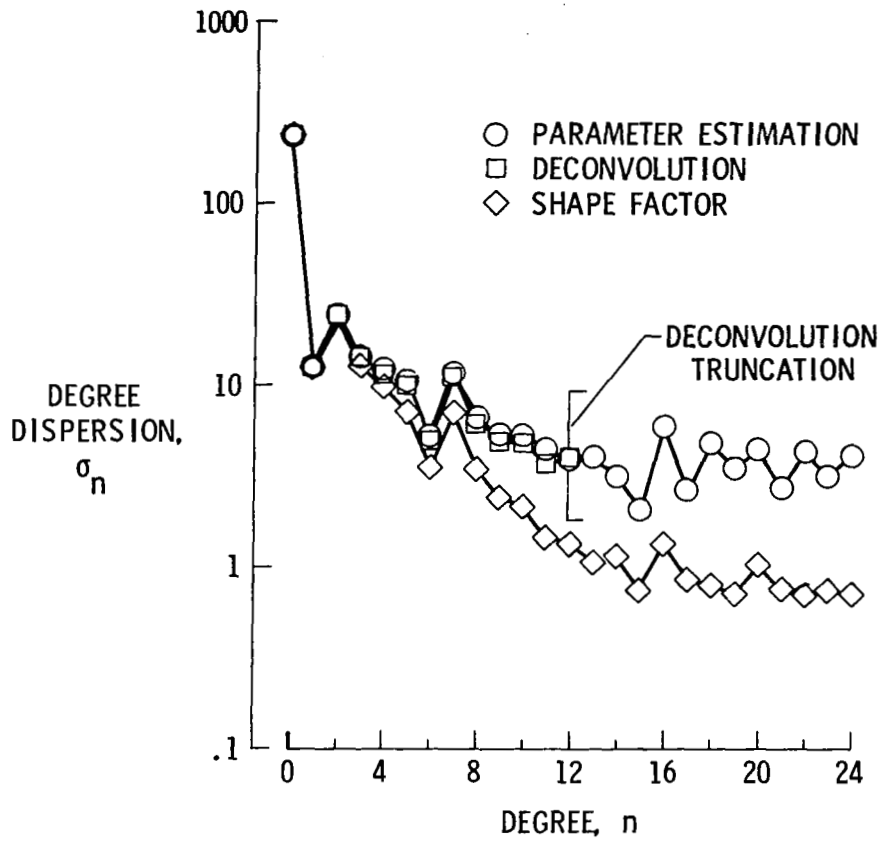

Figure 10.- Degree dispersion for the three techniques.

By comparing the spectral content of the three solutions, we conclude that the parameter estimation and deconvolution solutions are most similar on this basis to degree 12 and that the shape factor solution does not compare favorably with the other two solutions. Recall that the deconvolution technique enhances the high-frequency spatial components of the solution by dividing by a decreasing sequence of eigenvalues (eq. (20)). The shape factor technique, on the other hand, divides all measurements by a single shape factor (eq. (6)) which is equivalent to dividing all frequency components by the first eigenvalue λ_0 . Thus, the difference between the two spectra increases with degree. Since the wide field of view sensor smooths the measurements, it is reasoned that the deconvolution technique yields the more accurate solution. Although not explicit in the formulation, it can be concluded that the parameter estimation solution also enhances the high-frequency components, since it is so similar to the deconvolution solution. This enhancement was also demonstrated by Smith et al. (1975). Moreover, the 10° x 20° grid system does not seem to degrade the parameter estimation solution. It is remarkable that the spectra of the parameter estimation and deconvolution solutions are so similar considering that the spherical harmonic coefficients of the deconvolution solution were initially computed at satellite altitude with 5° x 5° regional data and the coefficients of the parameter estimation solution were computed at the top of the atmosphere with 10° x 20° regional values.

However, the parameter estimation and the deconvolution solutions do not compare favorably on a regional scale (from table V, the average regional difference is 8.60 $W\text{-}m^{-2}$). The problem results from the coordinate system transformations. The deconvolution solution is defined in terms of spherical harmonics. The parameter estimation solution is defined on a 10° × 20° grid system, converted to a 10° × 10° grid system, and then converted to a spherical harmonic representation. Traditionally, the transformation from regions to spherical harmonics has been considered valid to a degree number N equal to 180 divided by the region size, or N = 18 for 10° regions. Rapp (1977), however, has shown that this transformation can be expanded even beyond this degree. We have extended the transformation to N = 24 in figure 10 but have only compared to degree 12, since that is the limit of the deconvolution spectrum. Certainly the transformation from regions to spherical harmonics yields a spectrum of the parameter estimation solution reliable to degree 12. This is further substantiated by the favorable comparison of the two spectra. The regional comparison, on the other hand, necessitated transforming the deconvolution solution from spherical harmonics to regional values. Traditionally, this transformation is valid for grid sizes equal to 180 divided by N, or 15° regions for the 12th degree spherical harmonic expansion. Thus, the 12th degree spherical harmonic solution is not adequate to establish 10° regional values. Traditionally, a spherical harmonic expansion to degree 18 would be required to yield 10° regional values. Rapp finds that even an 18th degree expansion is inadequate and suggests that a 27th degree spherical harmonic expansion would be necessary to recover 10° regional values. Thus, the present deconvolution solution of degree 12 is quite insufficient to yield 10° regional values. For this reason the parameter estimation and deconvolution solutions do not compare favorably on a 10° × 10° grid system. Since only a 12th degree solution is available to define the regional values, they are smoothed because of the lack of the high-frequency terms. As previously discussed, the shape factor solution is also a smoothed representation, since it does not enhance the high-frequency components of the solution. Thus, these two smooth solutions, from the shape factor and deconvolution techniques, compare favorably on a regional basis. Nevertheless, the parameter estimation technique may give more reliable 10° × 10° regional values than either of these two smoothed solutions. However, because the true field is unknown, one cannot demonstrate the accuracy of any analysis technique on the basis of these results.

As previously discussed, use of 10° × 20° regions in the parameter estimation technique did not seem to degrade the spectrum of the solution, at least not to degree 12. From the deconvolution technique we can obtain the grid size resolution by the traditional method of dividing 180° by the degree number 12. This would imply that 15° × 15° regions, of which there are 185 to cover the globe, can be resolved. However, there are 208 regions of size 10° × 20° over the globe. Thus, we conclude that a 10° × 20° regional system is adequate.

The three numerical examples considered in this section are summarized in table VI. The sensitivity of the three techniques to the assumed directional function represents the difference in the solution using the Lambertian and limb darkening functions. The parameter estimation technique is more sensitive than the deconvolution technique. The shape factor technique is independent of directional function. The computer storage requirements and running times are also given for comparison and should be interpreted relatively, since the skill of the programmer and the type of computer affect these numbers. We can conclude, however, that the computational burden for the shape factor and deconvolution techniques is small compared with that for the parameter estimation technique. Since the quadrature scheme and the directional function greatly affect the computational burden, more detailed entries are given in table VI for the parameter estimation technique.

TABLE VI.- SUMMARY OF NUMERICAL EXAMPLE SOLUTIONS

Technique	Shape factor	Parameter estimation	Deconvolution
Algorithm	$\hat{M}(\theta_s,\Phi_s) = F^{-1}\, m(\theta_s,\Phi_s)$	$\hat{\underline{M}} = (B^TB)^{-1}B^T\underline{m}$	$\hat{M}(\theta,\Phi) = \sum_{n=0}^{N}\sum_{m=-n}^{n} \lambda_n^{-1} a_n^m Y_n^m(\theta,\Phi)$
Data processing	Individual	Batch	Batch
Data set	Averaged over 5° × 5° regions	Averaged over 5° × 5° regions	Averaged over 5° × 5° regions
Grid system	5° × 5° regions	10° × 20° regions	Spherical harmonics
Directional function, R	Homogeneous	Lambertian or limb darkening	Lambertian or limb darkening
Assumptions	1. Radiant exitance constant over FOV 2. Estimate associated with nadir point	1. Radiant exitance constant over 5° × 5° regions 2. R known for each grid region 3. Extrapolate 10° × 20° region to 10° × 10° region	1. Sensor response function of α only 2. R function of θ only and homogeneous over globe 3. Data defined on sphere 4. Solution truncated at N = 12
Sensitivity to directional function,[a] $W\text{-}m^{-2}$:			
Global difference	None	None	None
Zonal difference	None	0.85	0.55
10° regional difference	None	1.20	0.75
Computer storage	17 000	[b] 92 000 [c] 72 000	21 000
Computer running time, sec	1	L D: [b] 456 [c] 151 Lamb: [b] 335 [c] 120	5

[a] Difference between solutions with Lambertian and with limb darkening directional functions.
[b] For quadrature scheme with 2.5° subgrid.
[c] For quadrature scheme with 5° subgrid.

Finally, the advantages and disadvantages of the three techniques are summarized in table VII. The shape factor technique requires a minimim of computational time, is independent of the directional function, and does not require knowledge of the complete data set. The deconvolution technique is fast computationally, gives accurate spherical harmonic coefficients, and produces no quadrature errors. They both, however, have the disadvantage of inaccurate regional values. Other than the computational burden, the parameter estimation technique is impressive, yielding accurate spherical harmonic coefficients from 10° × 10° regional values. This implies that the regional values are reliable. Because the directional function can be defined at each quadrature subregion, the technique has considerable flexibility.

TABLE VII.- ADVANTAGES AND DISADVANTAGES OF TECHNIQUES

Technique	Advantages	Disadvantages
Shape factor	Simple, fast Requires little storage Popular Does not require complete data set Accurate global mean Independent of R Responds to local discontinuity	Does not enhance high frequency Inaccurate regional values Inaccurate high-frequency spherical harmonic components
Parameter estimation	Enhances high frequency Heterogeneous R over globe Accurate spherical harmonic coefficients	Requires large storage Requires complete data set Extrapolation from 10° × 20° regions to 10° × 10° regions Quadrature errors
Deconvolution	Fast Accurate spherical harmonic coefficients to degree 12 Requires little storage Enhances high frequency No quadrature errors	Inaccurate regional values Requires complete data set defined on sphere R function of θ only

CONCLUSIONS

Three data analysis techniques have been examined for estimating radiant exitance at the top of the atmosphere from Earth radiation budget observations. The shape factor, parameter estimation, and deconvolution techniques have been compared by examining their assumptions and characteristics, applying them to the same data set, and transforming their results to the same coordinate system.

The characteristics of the shape factor technique were examined by estimating the radiation field over a 5° and a 10° grid system. The difference between these two approaches was 0.30 $W\text{-}m^{-2}$ on a global scale and 0.83 $W\text{-}m^{-2}$ on a 10° regional scale. These results are independent of the directional function since we assumed the same directional function for all points on the globe. This assumption was shown to yield a shape factor which is independent of the directional function.

Two factors affect the radiation field derived by the parameter estimation technique: the directional function and the quadrature formula. The difference between using a Lambertian and a limb darkening function was negligible on a global scale and 1.20 $W\text{-}m^{-2}$ on a 10° regional scale. The difference between a 2.5° and a 5° quadrature scheme was 0.05 $W\text{-}m^{-2}$ on a global scale and 0.76 $W\text{-}m^{-2}$ on a 10° regional scale.

Implementation of the deconvolution technique requires that we define the directional function and that we truncate the spherical harmonic expansion at some finite degree. Neither one of these two factors affected the global average. On a 10° regional scale, the difference between using a Lambertian and a limb darkening function was 0.75 $W\text{-}m^{-2}$ and the difference between truncating the spherical harmonic expansion at degree 12 and at degree 15 was 3.94 $W\text{-}m^{-2}$. Thus, on a regional scale, the degree of truncation has more influence on the derived radiation field than the directional function.

The three data analysis techniques have been intercompared. All three techniques produced essentially the same estimate of the global radiant exitance. The two solutions that have the highest correlation on a 10° regional scale are the shape factor and deconvolution solutions. Their 10° regional difference is 5.95 $W\text{-}m^{-2}$. The favorable comparison of these two solutions is due to their smoothness. The shape factor smooths the solution by not enhancing the high spatial frequencies. The deconvolution technique smooths the solution by truncating the spherical harmonic representation at a finite degree.

Another comparison of the three solutions is made by examining their spatial spectra. The parameter estimation and the deconvolution spectra are very close out to degree 12 where the deconvolution spectrum is truncated. The shape factor spectrum gradually departs from these two spectra, the departure becoming large after degree 3. The parameter estimation and the deconvolution solutions do not compare favorably on a regional scale because the 12th degree spherical harmonic solution is not adequate to establish 10° regional values. However, their spatial spectra do compare favorably (out to degree 12) since 10° regional values yield a reliable spectra to degree 12. Even though the shape factor and the deconvolution solutions compare most favorably on a 10° regional scale, the parameter estimation technique may

give more reliable 10° regional values than either of the two smoothed solutions. However, because the true radiation field is unknown, one cannot demonstrate the accuracy of any of the three analysis techniques on the basis of these results.

Langley Research Center
National Aeronautics and Space Administration
Hampton, VA 23665
September 9, 1981

APPENDIX A

SPHERICAL HARMONIC COEFFICIENTS FROM REGIONAL VALUES

Consider the radiant exitance field over the globe in terms of regional values which are the average radiant exitances over the regions. A set of regional values can be transformed to spherical harmonic coefficients by the principle of orthogonal projection, that is,

$$\tilde{C}_n^m = \frac{1}{4\pi} \int_{\text{Sphere}} \tilde{X}(\Theta,\Phi)\, Y_{cn}^m(\Theta,\Phi)\, dA \tag{A1}$$

where $\tilde{C}_n^m$ are the spherical harmonic coefficients and $\tilde{X}(\Theta,\Phi)$ is known in terms of regional values. These coefficients, however, represent the averaged or smoothed field. To compute the original, or unsmoothed, coefficients from the regional values, $\tilde{C}_n^m$ must be increased, or enhanced, to represent the original field. The smoothing parameter β_n defined by Pellinen (1967) is used for this purpose. Following his approach, define the original spherical harmonic representation as

$$X(\Theta,\Phi) = \sum_{n=0}^{\infty} \sum_{m=0}^{n} N_n^m \left(C_n^m \cos m\Phi + S_n^m \sin m\Phi \right) P_n^m(\cos \Theta) \tag{A2}$$

and the spherical harmonic representation of the constant regional values which requires an infinite number of terms can be defined as

$$\tilde{X}(\Theta,\Phi) = \sum_{n=0}^{\infty} \sum_{m=0}^{n} N_n^m \left(\tilde{C}_n^m \cos m\Phi + \tilde{S}_n^m \sin m\Phi \right) P_n^m(\cos \Theta) \tag{A3}$$

where $\tilde{X}(\Theta,\Phi) = X_k$ is constant for $\Theta_{k1} \leq \Theta \leq \Theta_{k2}$ and $\Phi_{k1} \leq \Phi \leq \Phi_{k2}$. Rapp (1977) has shown that it is theoretically expedient to use a circular smoothing operator in place of the rectangular regional operator (eq. (30)). The angular radius of the circular region γ^* is chosen so that the areas of the circular region and the rectangular region are the same. This relationship is given by

$$\sin\left(\frac{\gamma^*}{2}\right) = \left(\frac{\Theta \sin \Theta}{4\pi}\right)^{1/2}$$

where Θ is the angular dimension of the rectangular region. A $10° \times 10°$ rectangular region corresponds to a circular region with $\gamma^* = 5.63°$.

The circular smoothing operator is similar to the rectangular smoothing operator (eq. (30)) and is given by

APPENDIX A

$$X_k = \frac{\int_{\beta=0}^{2\pi} \int_{\gamma=0}^{\gamma^*} X(\Theta,\Phi) \sin\gamma \, d\gamma \, d\beta}{\int_{\beta=0}^{2\pi} \int_{\gamma=0}^{\gamma^*} \sin\gamma \, d\gamma \, d\beta} \tag{A4}$$

where γ and β are the polar coordinates describing the circular region centered at $\Theta_k = \frac{\Theta_{k1} + \Theta_{k2}}{2}$ and $\Phi_k = \frac{\Phi_{k1} + \Phi_{k2}}{2}$. Pellinen presented the following relationship:

$$\int_{\gamma=0}^{\pi} \int_{\beta=0}^{2\pi} \rho(\gamma) \, P_n^m(\cos\Theta) \begin{Bmatrix} \sin m\Phi \\ \cos m\Phi \end{Bmatrix} \sin\gamma \, d\beta \, d\gamma$$

$$= 2\pi \, P_n^m(\cos\Theta_k) \begin{Bmatrix} \sin m\Phi_k \\ \cos m\Phi_k \end{Bmatrix} \int_{\gamma=0}^{\pi} \rho(\gamma) \, P_n^0(\cos\gamma) \sin\gamma \, d\gamma \tag{A5}$$

where the weighting function $\rho(\gamma)$ is taken as

$$\rho(\gamma) = \begin{cases} 1 & (0° \leq \gamma \leq \gamma^*) \\ 0 & (\text{Otherwise}) \end{cases}$$

Substituting equation (A2) into equation (A4) yields

$$X_k = \frac{\int_{\beta=0}^{2\pi} \int_{\gamma=0}^{\gamma^*} \sum_{n=0}^{\infty} \sum_{m=0}^{n} N_n^m \left(C_n^m \cos m\Phi + S_n^m \sin n\Phi \right) P_n^m(\cos\Theta) \sin\gamma \, d\gamma \, d\beta}{2\pi(1 - \cos\gamma^*)}$$

Simplifying with equation (A5) gives

$$X_k = \sum_{n=0}^{\infty} \sum_{m=0}^{n} \beta_n N_n^m \left(C_n^m \cos m\Phi_k + S_n^m \sin m\Phi_k \right) P_n^m\left(\cos\Theta_k\right) \tag{A6}$$

where

APPENDIX A

$$\beta_n = \frac{1}{1 - \cos \gamma^*} \int_{\gamma=0}^{\gamma^*} P_n^0(\cos \gamma) \sin \gamma \, d\gamma$$

Using

$$P_n(x) = \frac{1}{2n + 1}\left[\frac{d}{dx} P_{n+1}(x) - \frac{d}{dx} P_{n-1}(x)\right]$$

we can express the smoothing parameter β_n as

$$\beta_n = \frac{1}{1 - \cos \gamma^*} \frac{1}{2n + 1}\left[P_{n-1}(\cos \gamma^*) - P_{n+1}(\cos \gamma^*)\right] \qquad (n = 1, 2, \ldots)$$

and $\beta_0 = 1$.

Now X_k in equation (A6) represents the average over a circular region centered at Θ_k and Φ_k. If this expression is used to approximate the average over a rectangular region, then we substitute X_k for $\tilde{X}(\Theta,\Phi)$ in equation (A3) and by comparing coefficients obtain $\tilde{C}_n^m = \beta_n C_n^m$ and $\tilde{S}_n^m = \beta_n S_n^m$. Thus, the original spherical harmonic representation denoted by C_n^m and S_n^m is smoothed by the parameter β_n when averaged over a region. To compute the original spherical harmonic coefficients C_n^m and S_n^m from the regional values, we first must calculate the spherical harmonic coefficients $\tilde{C}_n^m$ and $\tilde{S}_n^m$ that represent the smooth field by equation (A1) and then divide them by β_n; that is, $C_n^m = \beta_n^{-1}\tilde{C}_n^m$ and $S_n^m = \beta_n^{-1}\tilde{S}_n^m$. It is interesting to note that as a result of equation (A5), β_n is a function of degree n but not a function of order m of the spherical harmonic. The smoothing parameter β_n is presented in figure 3 for two values of γ^*.

APPENDIX B

10° × 10° REGIONAL VALUES FROM 10° × 20° REGIONAL VALUES

In this appendix, a formula for estimating 10° × 10° regional radiant exitances from 10° × 20° regional radiant exitances is derived on a zonal basis so that the 10° × 20° regional estimate of one zone affects only the 10° × 10° regional estimates of that zone. The criterion for dividing the estimate is that the sum of the slopes squared around the zone is a minimum. This yields the solution with lowest spatial frequency. Consider a zone composed of 10° × 20° regions, where the radiant exitances are denoted by $M_1, M_2, \ldots, M_n$. Further let us define the 10° × 10° radiant estimates by $M_{11}, M_{12}, M_{21}, M_{22}, \ldots, M_{n2}$, where M_{i1} corresponds to the western half of the ith region and M_{i2} corresponds to the eastern half. Thus, $M_i = (1/2)(M_{i1} + M_{i2})$. The following diagram is helpful:

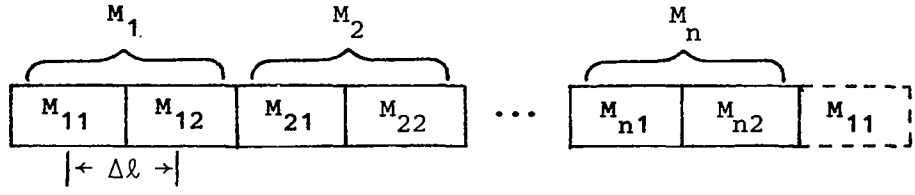

The sum of the slopes squared S is

$$S = \left(\frac{M_{12} - M_{11}}{\Delta\ell}\right)^2 + \left(\frac{M_{21} - M_{12}}{\Delta\ell}\right)^2 + \ldots + \left(\frac{M_{11} - M_{n2}}{\Delta\ell}\right)^2$$

Substituting the relation $M_{i2} = 2M_i - M_{i1}$ gives

$$S = \left(\frac{2M_1 - 2M_{11}}{\Delta\ell}\right)^2 + \left(\frac{M_{21} - 2M_1 + M_{11}}{\Delta\ell}\right)^2 + \ldots + \left(\frac{M_{11} - 2M_n + M_{n1}}{\Delta\ell}\right)^2$$

or in matrix form

$$S = 8M^TM + 6X^TX - 12X^TM + 2X^TPX - 4X^TP^TM$$

where

$$M^T = [M_1 \quad M_2 \quad \cdots \quad M_n]$$

$$X^T = [M_{11} \quad M_{21} \quad \cdots \quad M_{n1}]$$

$$P = \begin{bmatrix} 0 & 1 & 0 & \cdots & 0 \\ 0 & 0 & 1 & \cdots & 0 \\ \cdot & \cdot & \cdot & \cdot & \cdot \\ \cdot & \cdot & \cdot & \cdot & \cdot \\ \cdot & \cdot & \cdot & \cdot & \cdot \\ 0 & 0 & 0 & \cdots & 1 \\ 1 & 0 & 0 & \cdots & 0 \end{bmatrix}$$

Since we desire to minimize S with respect to X,

$$\frac{dS}{dX} = 12X - 12M + 2PX + 2P^TX - 4P^TM = 0$$

or

$$(6I + P + P^T)X = (6I + 2P^T)M \tag{B1}$$

The solution of equation (B1) for X defines M_{i1} $(i = 1, 2, \ldots, n)$, and $M_{i2} = 2M_i - M_{i1}$. These are the 10° × 10° regional radiant exitances that minimize the sum of the slopes squared and give the smoothest curve through the data. Solving equation (B1) for $n = 4$ gives

$$M_{i1} = \frac{1}{6}(M_{i-1} + 6M_i - M_{i+1}) \qquad (i = 1, 2, 3, 4) \tag{B2}$$

where $M_0 = M_n$ and $M_{n+1} = M_1$. For $n = 5$,

$$M_{i1} = \frac{1}{29}(-M_{i-2} + 5M_{i-1} + 29M_i - 5M_{i+1} + M_{i+2}) \qquad (i = 1, 2, \ldots, 5)$$

where $M_{-1} = M_{n-1}$ and $M_{n+2} = M_2$. For this study we have approximated the solution to equation (B1) by equation (B2) for all n.

APPENDIX C

SPECTRUM OF A RANDOM FIELD

The interpretation of a nearly constant spectrum as random noise is illustrated by examining the spectrum of a random field. Define the random field by 5° × 5° regional values X_k, where X_k is a normal random variable with mean zero and variance σ^2. Also define $E[X_k X_j] = \delta_k^j \sigma^2$, which is the regional equivalent of white noise. From appendix A the spherical harmonic coefficients for this random field are

$$C_n^m = \frac{1}{4\pi\beta_n} \sum_{k=1}^{K} X_k \int_{\text{Region } k} Y_{cn}^m(\Theta,\Phi)\, dA$$

and

$$\left(C_n^m\right)^2 = \left(\frac{1}{4\pi\beta_n}\right)^2 \sum_{k=1}^{K} \sum_{j=1}^{K} X_k X_j \int_{\text{Region } k} \int_{\text{Region } j} Y_{cn}^m(\Theta,\Phi)\, Y_{cn}^m(\Theta',\Phi')\, dA\, dA'$$

and the expected value of $\left(C_n^m\right)^2$ is

$$E\left[\left(C_n^m\right)^2\right] = \left(\frac{\sigma}{4\pi\beta_n}\right)^2 \sum_{k=1}^{K} \left[\int_{\text{Region } k} Y_{cn}^m(\Theta,\Phi)\, dA\right]^2 \tag{C1}$$

We derive a similar expression for $E[(S_n^m)^2]$ and define

$$E\left[\sigma_n^2\right] = \sum_{m=0}^{n} \left\{E\left[\left(C_n^m\right)^2\right] + E\left[\left(S_n^m\right)^2\right]\right\} \tag{C2}$$

which is represented in figure 6 for $\sigma = 10$ W-m^{-2}. Although the spectrum for the random field gradually increases for $n > 15$, it supports the interpretation of a constant spectrum as noise. Note that if the regions are sufficiently small so that Y_{cn}^m can be assumed constant over the region, then

$$\left[\int_{\text{Region } k} Y_{cn}^m(\Theta,\Phi)\, dA\right]^2 = \left(Y_{cn}^m\right)^2 A_k^2 = A_k \int_{\text{Region } k} \left(Y_{cn}^m\right)^2 dA$$

and equation (C1) becomes

APPENDIX C

$$E\left[\left(C_n^m\right)^2\right] = \left(\frac{\sigma}{4\pi\beta_n}\right)^2 \sum_{k=1}^{K} A_k \int_{\text{Region } k} \left(Y_{cn}^m\right)^2 dA$$

For small regions the smoothing parameter β_n is approximately unity for all n. Also, if we assume all areas to be equal, that is, $A_k = A = 4\pi/K$, and make use of the orthogonality condition (eq. (23)), then

$$E\left[\left(C_n^m\right)^2\right] = \left(\frac{\sigma}{4\pi}\right)^2 A \int_{\text{Sphere}} \left(Y_{cn}^m\right)^2 dA = \frac{\sigma^2}{K}$$

with a similar expression for $E[(S_n^m)^2]$, the expected value of the degree variance for small regions is approximately given by

$$E\left[\sigma_n^2\right] \approx \frac{(2n + 1)\sigma^2}{K} \tag{C3}$$

Thus, the spectrum of a random field defined on a regional grid system is proportional to $\sqrt{2n + 1}$, and for a 5° × 5° regional grid system the spectra given by equations (C2) and (C3) are indistinguishable.

REFERENCES

Bess, T. Dale; Green, Richard N.; and Smith, G. Louis 1981: Deconvolution of Wide Field-of-View Radiometer Measurements of Earth-Emitted Radiation. Part II: Analysis of First Year of Nimbus 6 ERB Data. J. Atmos. Sci., vol. 38, no. 3, pp. 474-488.

Green, Richard N. 1981: Simulation of a Numerical Filter for Enhancing Earth Radiation Budget Measurements. Fourth Conference on Atmospheric Radiation, American Meteorol. Soc., pp. 153-160.

Jacobowitz, H.; Smith, W. L.; Howell, H. B.; Nagle, F. W.; and Hickey, J. R. 1979: The First 18 Months of Planetary Radiation Budget Measurements From the Nimbus 6 ERB Experiment. J. Atmos. Sci., vol. 36, no. 3, pp. 501-507.

Pellinen, L. P. 1967: A Method for Expanding the Gravity Potential of the Earth in Spherical Functions. Research in Geodetic Gravimetry and Theory of the Earth's Figure. ACIC-TC-1282, Aeronaut. Chart & Inform. Center, pp. 65-116. (Available from DTIC as AD 661-810.)

Rapp, Richard H. 1977: The Relationship Between Mean Anomaly Block Sizes and Spherical Harmonic Representations. J. Geophys. Res., vol. 82, no. 33, pp. 5360-5364.

Raschke, Ehrhard; Vonder Haar, Thomas H.; Pasternak, Musa; and Bandeen, William R. 1973: The Radiation Balance of the Earth-Atmosphere System From Nimbus 3 Radiation Measurements. NASA TN D-7249.

Smith, G. Louis; and Green, Richard N. 1981: Deconvolution of Wide Field-of-View Radiometer Measurements of Earth-Emitted Radiation. Part I: Theory. J. Atmos. Sci., vol. 38, no. 3, pp. 461-473.

Smith, G. Louis; Green, Richard N.; and Campbell, G. G. 1975: A Statistical Interpretation Technique for Wide Angle Radiometer Measurements of Earth Energy Budget. Fourth Conference on Probability and Statistics in Atmospheric Science, American Meteorol. Soc., pp. 171-176.

Smith, W. L.; Hickey, J.; Howell, H. B.; Jacobowitz, H.; Hilleary, D. T.; and Drummond, A. J. 1977: Nimbus-6 Earth Radiation Budget Experiment. Appl. Opt., vol. 16, no. 2, pp. 306-318.

Weaver, William L.; and Green, Richard N. 1980: Simulation Study of a Geometric Shape Factor Technique for Estimating Earth-Emitted Radiant Flux Densities From Wide-Field-of-View Radiation Measurements. NASA TP-1629.

Weaver, William L.; and House, Frederick B. 1979: Analyses of Earth Radiation Budget Data From Unrestricted Broadband Radiometers on the ESSA 7 Satellite. NASA TP-1402.

1. Report No.	2. Government Accession No.	3. Recipient's Catalog No.
NASA TP-1924		

4. Title and Subtitle	5. Report Date
COMPARISON OF DATA INVERSION TECHNIQUES FOR REMOTELY SENSED WIDE-ANGLE OBSERVATIONS OF EARTH EMITTED RADIATION	December 1981
	6. Performing Organization Code: 146-10-06-02
7. Author(s): Richard N. Green	8. Performing Organization Report No.: L-14591
	10. Work Unit No.
9. Performing Organization Name and Address: NASA Langley Research Center, Hampton, VA 23665	11. Contract or Grant No.
	13. Type of Report and Period Covered: Technical Paper
12. Sponsoring Agency Name and Address: National Aeronautics and Space Administration, Washington, DC 20546	14. Sponsoring Agency Code

15. *Supplementary Notes*

16. Abstract

Three different data analysis techniques - shape factor, parameter estimation, and deconvolution - have been applied to the same set of Earth emitted radiation measurements to determine the effects of different techniques on the estimated radiation field. These measurements are from the Earth Radiation Budget (ERB) instrument aboard the Nimbus 6 satellite. With the shape factor technique, each measurement is divided by a scalar to estimate the radiant exitance at the top of the atmosphere. With the parameter estimation technique, all measurements are processed together as a batch and the derived radiant exitance is defined as a least squares fit to the data. With the deconvolution technique, use is made of the fact that spherical harmonics are the eigenfunctions of the measurement operator to derive the radiant exitance. All three techniques are defined and their assumptions, advantages, and disadvantages are discussed. Their results are compared globally, zonally, regionally, and on a spatial spectrum basis. The standard deviations of the regional differences in the derived radiant exitance varied from 7.4 $W\text{-}m^{-2}$ to 13.5 $W\text{-}m^{-2}$.

17. Key Words (Suggested by Author(s))	18. Distribution Statement
Earth radiation budget Inversion methods Parameter estimation Deconvolution Shape factor technique Data analysis	Unclassified - Unlimited Subject Category 47

19. Security Classif. (of this report)	20. Security Classif. (of this page)	21. No. of Pages	22. Price
Unclassified	Unclassified	45	A03

For sale by the National Technical Information Service, Springfield, Virginia 22161

NASA-Langley, 1981